Western Graduate&PostdoctoralStudies

Western University

Scholarship@Western

Electronic Thesis and Dissertation Repository

10-16-2018 2:00 PM

Validation of a Hyperspectral NIRS Method for Measuring Tissue Oxygen Saturation

Matthew Kewin
The University of Western Ontario

Supervisor
St Lawrence, Keith
The University of Western Ontario Co-Supervisor
de Ribaupierre, Sandrine
The University of Western Ontario

Follow this and additional works at: https://ir.lib.uwo.ca/etd

Part of the Medical Biophysics Commons

Abstract

Brain injury during preterm infancy can cause serious intellectual and behavioral disabilities, as such, measurements of cerebral health are needed to aid in the diagnosis and treatment of these injuries. Near infrared spectroscopy (NIRS) is considered ideal for this purpose because it is non-invasive and provides a continuous measure of tissue oxygen saturation (StO_2), a key marker of cerebral health. Current commercial NIRS systems have considerable variability between devices and between infants restricting them to monitoring trends. Time-resolved (TR) NIRS is considered the gold standard in biomedical optics for quantifying tissue optical properties, but the technology is more complex and has struggled with integration into clinical settings. As an inexpensive alternative, the present study investigated using a hyperspectral NIRS (H-NIRS) method to quantify StO_2. Experiments were conducted using newborn piglets and StO_2 measured at different oxygenation levels by H-NIRS and by TR-NIRS for validation. Measurements were acquired at step-wise reduction in StO_2 caused by reducing the fraction of inspired oxygen. Across eight animals, there was no significant effect between StO_2 measurements from the two techniques ($F_{5,35} = 1.591$, $p > 0.05$). The strong agreement ($R^2 = 0.95$) in the StO_2 measurements suggests that H-NIRS is a strong candidate for clinical use considering it is both quantitative and technically simple.

Keywords

Acknowledgments

Table of Contents

List of Tables

List of Figures

List of Abbreviations

NICU	Neonatal intensive care unit
VLBW	Very low birth weight
CBF	Cerebral blood flow
IVH	Intraventricular hemorrhage
PHVD	post hemorrhagic ventricular dilatation
CSF	Cerebral spinal fluid
cUS	Cerebral Ultrasound
ICP	Intracranial pressure
StO_2	Tissue oxygen saturation
NIRS	Near infrared spectroscopy
HbO_2	Oxy-hemoglobin
HHB	Deoxy-hemoglobin
$PaCO_2$	Arterial partial pressure of CO_2
RTE	Radiative transfer equation
WF	Water fraction
CW	Continuous wave
SRS	Spatially resolved spectroscopy
TR	Time Resolved
TPSF	Temporal point spread function
FD	Frequency domain
H	Hyperspectral
DCS	Diffuse correlation spectroscopy
CCO	Cytochrome-C-oxidase
HR	Heart rate
SaO_2	Arterial oxygen saturation

PaO$_2$	Arterial partial pressure of oxygen
FiO$_2$	Fraction of inspired oxygen
IRF	Impulse response function
COV	Coefficient of variance
ICG	Indocyanine green

<div align="center">Chapter 1</div>

1 Introduction

1.1 Rationale

The development of the modern neonatal intensive care unit (NICU) has led to significant decreases in the mortality and morbidity associated with very low birth-weight (VLBW) neonates (<1500g)[1]. Unfortunately, approximately 50% of VLBW neonates in Canada will either die during the neonatal period or survive with significant complications that can lead to long-term adverse consequences. Beyond the neonatal period of life, cognitive developmental issues and social and behavioral problems are prevalent, often related to considerable costs to these individuals and society as a whole[2]. The brains of VLBW neonates are particularly vulnerable to injury because their cerebral vasculature remains underdeveloped, making them fragile and susceptible to rupture[3]. This fact in conjunction with extremely low cerebral blood flows (CBF) and the inability to regulate CBF during changes of systemic pressure make these infants particularly vulnerable to tissue ischemia or vessel hemorrhage[4]. One of the major neonatal morbidities afflicting VLBW infants is intraventricular hemorrhage (IVH), which is linked to various developmental disabilities[5].

Intraventricular hemorrhage refers to a bleed situated within the lateral cerebral ventricles, and it is the most prevalent form of intracranial hemorrhage, occurring in at least 25% of Canadian VLBW neonates[6]. The incidence and severity of IVH are strongly correlated with younger gestational age as well as lower birth weight[7]. Prognosis is worse if post hemorrhagic ventricular dilatation (PHVD) occurs, which refers to the expansion of the ventricles due to clots and blood breakdown products from the initial bleed blocking the normal circulation of cerebral spinal fluid (CSF). Enlarged ventricles increase intracranial pressure, leading to subsequent brain injury following the initial bleed. The occurrence of PHVD is associated with developmental delay, auditory and visual deficits, cerebral palsy, and even death in severe cases[8].

Intraventricular hemorrhage typically occurs within the first three days of life, and these infants are closely monitored afterwards to track bleeding and the potential onset of PHVD. Although the disease mechanisms are not completely understood, one of the major contributing factors is believed to be the combination of impaired cerebral autoregulation, which is the ability of the cerebrovascular system to regulate its blood flow despite fluctuations in blood pressure, and the presence of fragile vessels within the germinal matrix of the premature brain. The germinal matrix is a highly vascularized structure located directly adjacent to the lateral ventricles and is an express site of cell division and migration as precursor cells are generated and brought to the cerebral cortex. The vessels in the germinal matrix are not structurally sound when compared to more developed vessels and therefore susceptible to hemorrhage if exposed to fluctuations in blood pressure and flow[3]. Unfortunately, the fragility of these vessels is compounded by the fact that many preterm infants have poor cerebral autoregulation and therefore fluctuations in blood flow are common due to changes in systemic blood pressure[4].

Imaging the neonatal brain to monitor different pathologies has complications because neonates are typically bound to incubators requiring ventilation for immature lungs, temperature control and IVs for nutrition or treatment for other co-morbidities. Consequently, there is a need for modalities that can be used at the bedside. MRI compatible incubators exist in research centers and are of clinical and research interest. Neonates still need to be transferred to this incubator which has risks, and there are considerable costs due to need for MRI compatible equipment and personnel.

Cranial ultrasound (cUS) is used to diagnose and monitor the progression of IVH. In addition, it is used to help detect the onset of PHVD by tracking the size of the ventricles. cUS is performed via the anterior fontanelle which acts an acoustic window for imaging where the ventricles appear black due to their low scatter, a solid blood clot from IVH appears white and the surrounding brain tissue is grey in colour. The width of the ventricles in this para-coronal plane and the thalamo-occipital distance are used to track the ventricle dilatation. These quantitative measurements are more valuable than qualitative estimates of ventricle size; however, suffer from intra and inter-subject

variation of each measurement. Furthermore, using linear measurements from 2D ultrasound to quantify irregularly shaped 3D ventricles is a fundamental limitation.

Other clinical markers of PHVD include expanding head circumference, tensing of fontanelles, separation of cranial suture, and symptoms of increased intracranial pressure (ICP; apnea, vomiting, bradycardia, abnormal posture)[9]. The ultimate treatment for PHVD is the insertion of a ventriculo-peritoneal shunt to divert accumulating CSF away from the brain[10]. However, this intervention is often delayed after initial diagnosis to allow time for blood clots and CSF protein levels to decrease so that the shunt will not be blocked. During this waiting period, interventions including lumbar punctures if CSF communication remains or a ventricular tap, which refers to the removal of CSF by needle aspiration, may be required to relieve elevated ICP and reduce the risk of brain damage. These interventions are associated with their own risks, in particular the risk of infection, and therefore the frequency and number of taps needs to be carefully assessed based on clinical symptoms[11]. Continuous monitoring of ventricle size and head circumference is suggested as dilatation may stop naturally. However, there is currently no consensus on how and when to treat neonates with PHVD in a manner that optimizes neurological outcomes and quality of life.

3D US has been developed to measure ventricle volume and studies have suggested that 2D US measurements may not track progressively dilating vessels accurately[12]. It has been described that cerebral hemodynamic and metabolic disruption occur before elevated ICP is clinically detected. Amplitude-integrated electroencephalography has been used to report abnormal background electrical pattern's prior to ventricular dilation or clinical decline in neonates with PHVD, and a return to normal patterns after CSF removal[13]. Additionally, increased regional tissue oxygen saturation (StO_2) measured by near-infrared spectroscopy (NIRS) has been reported after ventricular taping[14]. These findings indicate that assessing oxygen delivery and cerebral energy metabolism could aid in treatment decisions of PHVD and improve neurological outcomes.[15]. NIRS is a promising tool due to its availability for measurements within the incubator, its non-invasive nature, and ability to measure cerebral hemodynamics.

1.2 Near-Infrared Spectroscopy

Near-infrared spectroscopy (NIRS) refers to non-invasive techniques that interrogate tissues by light to measure concentrations of light-absorbing molecules called chromophores. These methods take advantage of the low absorption in tissue of light in the near infrared range (650-1000 nm). Consequently, penetration depths on the scale of centimeters can be achieved. In this window, there are only a few endogenous chromophores that can be characterized by distinct absorption spectra. The most significant endogenous chromophores are water, oxyhemoglobin (HbO_2) and deoxyhemoglobin (HHb). Their specific absorption spectra are displayed in figure 1-1.
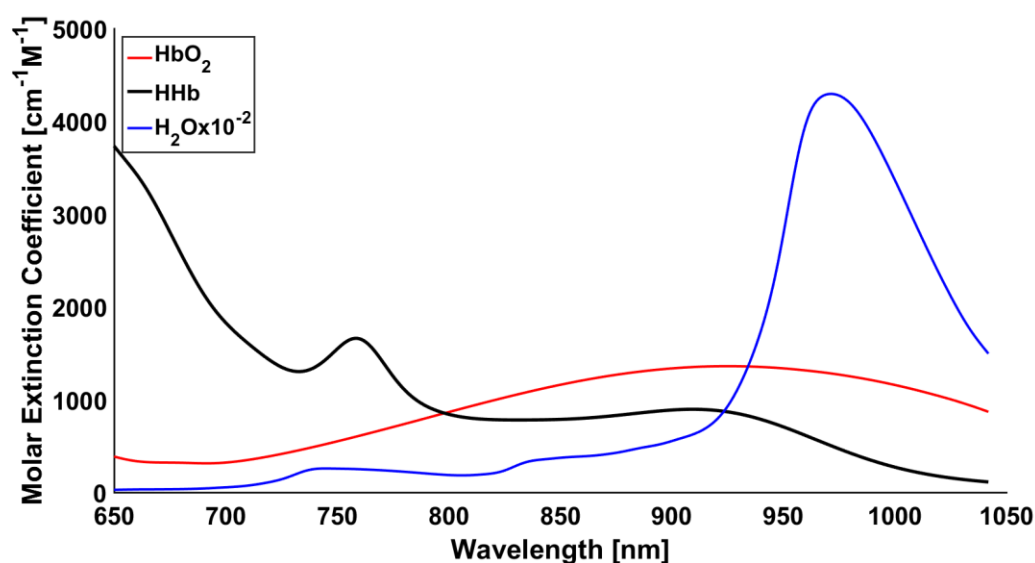
Figure 1-1 Molar extinction coefficients for the three most important endogenous NIR chromophores: deoxyhemoglobin (HHb), oxyhemoglobin (HbO_2), and water, which is scaled by 100 for display purposes.

Hemoglobin is the most relevant endogenous chromophore because of its strong absorption properties and because the absorption spectra changes with oxidation state. This is the driving property of NIRS as it allows the concentrations of HbO_2 and HHb to

be isolated if absorption is measured at two or more wavelengths. These are most often combined to measure tissue oxygen saturation:

$$StO_2 = \frac{[HbO_2]}{[HbO_2] + [HHb]}$$ (1.1)

1.2.1   The Clinical Applications of NIRS in Preterm Infants

The first application of NIRS with preterm infants was published in 1985, in which they reported correlations between apnea and transcutaneous oxygen measured on one side of the head, and HbO_2 and cytochrome oxidase (CCO), which is a marker of oxidative metabolism, measured by NIRS on the opposite side of the brain[16]. Shortly thereafter, a correlation between arterial partial pressure of CO_2 ($PaCO_2$) and NIRS measurements of cerebral blood volume and cerebral oxygenation index was demonstrated[17]. These early studies suggested that NIRS could be an ideal neuromonitoring tool for preterm infants since the technology appeared to be sensitive to cerebral hemodynamics changes and there was minimal signal contamination from extracerebral tissue (skin, scalp, skull) at this early age. The promise of these initial applications has led to a tremendous growth in NIRS as a research tool for studies of neonatal brain injury.

In general, clinical studies have shown that cerebral oxygenation measured by NIRS changes in the expected direction; however, absolute values have been inconsistent across studies and between different devices[18,19]. In comparison studies of some of the most commonly used commercial NIRS devices, differences in StO_2 range typically from 10 to 15 %, but up to 20% at low StO_2 values[19]. This variability across devices makes it difficult to establish StO_2 thresholds that can guide clinical management. Recent work determined equations to convert values from one device to another in an effort to standardized oxygenation measurements across different devices[18]. The question remains how to determine the true physiological value. Ideally, these monitors will be able to

display the current tissue oxygenation value, the trends, and a well-defined alarm when values are exiting an established safe range.

A concern with this concept of a monitoring target is that cerebral oxygenation is not a well-defined physiological quantity to establish thresholds because there is not a true gold standard measurement technique. The most common validation of StO_2 in the brain involves comparisons to arterial saturation or to venous saturation from the jugular bulb or the sagittal sinus. The problem with these validations are that NIRS estimates of arterial saturation depend on assumptions of an arterial-to-venous ratio in tissue which can very amongst individuals[18]. Also, venous samples may be inaccurate because at times some tissue regions will have lower oxygenation than the venous sample because of the heterogeneity in cerebral metabolism and the pooled venous blood from different brain regions coming together.

Therefore, a target range of oxygenation may need to be determined empirically and defined by construct validity. In 2015, population-based reference ranges were published using a commercially available device[20]. In this study a large number of preterm infants were monitored in the first three days of life, and significant differences were seen based on gestational age, sex, day after birth, and size relative to gestational age norms. A problem with these specific references is that the reference cerebral oxygenation range is lower for infants at a lesser gestational age, while their risk for brain injury is higher, and this increased risk could be due to that lower observed range. Experimental thresholds have also been examined using newborn piglets as an experimental model. These studies explored the lower StO_2 limit when cerebral metabolites were maintained within normal ranges, as well as the values and time scales required to cause mitochondrial damage and neuronal death[21–23]. However, piglets typically have a more developed brain at birth, so these thresholds may not be directly translatable to preterm infants. However, both of these approaches found a lower StO_2 threshold of approximately 55%.

Exploring these threshold values is a good start; however as stated above, with the variability between devices and no gold standard for saturation measurements, there is

further work to be done. An additional issue is the precision of many of these devices; that is, how reproducible are the results from a single device. An initial study indicated that repeatedly placing and replacing NIRS probes resulted in a precision standard deviation of approximately 5% which results in a repeatability coefficient of 14 %[24]. This level of imprecision is troubling when normal saturations values may be approximately 70% and the lower threshold for concern is 55%. However, the use of NIRS has made major strides towards becoming valuable in the NICU, including improved probe designs to reduce repeatability measurements and multi-center clinical trials to explore the benefit of monitoring StO_2 with evidence-based treatment guidelines[25,26]. For example, the SafeBoosC-II trial demonstrated a reduced burden of cerebral hypoxia in preterm infants in their first three days of life by adding cerebral oximetry to their standard of care[27].

1.2.2   Physical Principles of NIRS

As light propagates through tissue, it becomes attenuated because of the effects of absorption and scatter. The absorption from a volume sample of tissue is a result of the wavelength dependent properties of the constituent molecules. This is the most relevant property of biomedical NIRS applications because the absorption of a sample is directly related to the concentrations of the chromophores within. However, it is scatter that is the most abundant interaction between light and tissue, occurring approximately ten times for every absorbing event and is dependent on the wavelength of light and size of the scattering particles. Therefore, in order to extract valuable information from the attenuation of light, both scattering and absorption effects need to be taken into account.

Absorption is the transfer of light energy to the internal energy of atoms and molecules in tissue. Photons with particular frequencies excite electrons to excited states; the energy is then converted to heat as the electrons return to their ground states. The frequencies of light that are absorbed by a molecule depend on the structure of the molecule[28].

In a non-scattering medium, absorption is the reduction of light intensity as it passes through the medium. In 1729, Bouguer was the first to record this phenomenon, while Lambert extended this finding to state that the absorbance was directly proportional to the

thickness of the sample or the light's path length. The amount of light that is absorbed dI/I is proportional to the thickness of a small layer, dl, by a constant proportionality constant μ_a. The Lambert-Bouguer law was extended in 1852 by Beer who related μ_a to the concentration of a light absorber in the medium, c, producing the Beer-Lambert law:

$$A = -\log\left(\frac{I}{I_o}\right) = \mu_a l = \varepsilon c l \tag{1.2}$$

where, A is the absorbance and ε is the molar extinction coefficient of a chromophore with concentration c. When a sample is composed of multiple absorbers, this equation can be expanded linearly to be the sum of all constituent absorbers as follows:

$$A = \sum_i \varepsilon_i \cdot c_i \cdot l \tag{1.3}$$

Light scattering occurs when light is redirected from its initial path as a result of differences of refractive index, without a change in the energy of the incident light. As light moves through tissues it encounters tissue-tissue boundaries, cell membranes and organelles, and will be reflected, refracted or redirected at each of these interfaces. The degree to which light is scattered is a function of the density of particles, the size of the particles with respect to the wavelength of light, and the ratio of the refractive index of these particles compared to that of the surrounding medium. Light scatter can be considered in three main cases: scattering by particles that are small compared to the wavelength of light (Rayleigh scattering), larger structures (Mie scattering), and at interfaces between media with differing indices of refraction (Fresnel reflection). In the NIR range, Mie scattering and Fresnel reflection are dominant, with Rayleigh scattering becoming more relevant with decreasing wavelength. Owing to the large number of tissue-tissue boundaries and cell membranes that are larger than the wavelength of light, scatter is best described statistically. The attenuation of light due to scatter can be described mathematically by an exponential decay:

$$I = I_o e^{-\mu_s l} \tag{1.4}$$

where, μ_s is the scattering coefficient which represents the probability that a photon will experience scatter per unit length. The intensity, I, is a measure of non-scattered light and is a function of direction, area, and position. In tissue the probability of scattering event is far larger than that of an absorbing event, this leads to multiple scattering events that causes photons to become totally randomized with respect to their direction and the light can be considered diffuse.

To properly characterize the actions of light in tissue, the directionality of scatter needs to be considered. The scattering of light in tissue is not isotropic and instead is strongly forward scattering, which can be quantified using the anisotropy factor, g, representing the amount of forward direction retained and is the mean cosine of the scattering angle. In a medium where scattering events greatly outnumber absorbing, like in tissue, light transport can be described by diffusion. In the diffusive regime, it is useful to assume non-directional scattering, with a reduction in the probability of scattering coefficient by a factor of 1-g. This scaled probability is known as the reduced scattering coefficient and describes the diffusion of photons through a random walk process.

$$\mu'_s = \mu_s(1 - g) \tag{1.5}$$

It has been shown that for wavelengths relevant to NIRS in tissue, the change in the reduced scattering coefficient with respect to wavelength can be well described by a power law:

$$\mu'_s(\lambda) = \beta \left(\frac{\lambda}{\lambda_o}\right)^{-\alpha} \tag{1.6}$$

where β and α are constants determined experimentally or predicted through Mie scattering.

9

Performing quantitative spectroscopy (i.e., measuring the concentration of tissue chromophores) requires accounting for the dominant effect of light scattering. One empirical approach, which is referred to as the modified Beer-Lambert law, is given by:

$$A(\lambda) = DP(\lambda) \sum_i \varepsilon_i c_i + G(\lambda). \tag{1.7}$$

The modifications to this equation are that A now refers to total light attenuation with respect to wavelength λ; a scalar term, $G(\lambda)$, accounts for the portion of light that is not detected due to scatter; and DP is the differential pathlength, which takes into account that due to multiple scattering events the distance traveled by light is greater than the source detector distance. This differential pathlength is dependent on the interrogated media's μ'_s.[29] These modifications can complicate the ability to measure the concentrations of light absorbers in tissue because the observed attenuation is no longer directly related to μ_a. Relative changes can be determined if it is assumed that the attenuation due to scatter is constant. To extract concentrations from this equation or to track changes in concentrations requires determining DP, which can be obtained by modeling light transport in tissue and is outlined in the following section.

1.3   Modeling light propagation in tissue

Determining the optical properties of tissue or any turbid medium from propagated light requires solving an inverse problem where the interactions with light need to be extracted from the changes in light that has traversed the medium. Scattered light can be measured either in a reflectance geometry, where source and detector are on the same side, or in a transmission geometry, where source and detector are on opposite sides. In applications focused on brain monitoring, reflectance geometries are most commonly used because transmitted light can only be detected through the smallest of head circumferences. Reflectance ($R(\lambda)$) can be described mathematically as:

$$R(\lambda) = \left(\frac{I}{I_o}\right) \qquad (1.8)$$

Where I is the detected light and I_o is the reference light that is incident on the sample.

The behavior of light in tissue, as with all electromagnetic radiation, is dictated by the physics described by Maxwell's equations. Unfortunately, heterogeneous, highly scattering media with complex geometries like that of tissue make analytical solutions to these equations near impossible. These issues can be overcome by treating the light as individual photons that are elastically scattered and absorbed and driven by the radiative transfer equation (RTE):

$$\left[\frac{1}{v}\frac{\delta}{\delta t} + \hat{s}\cdot\nabla + \mu_a + \mu_s\right]L(r,t,\hat{s})$$
$$= \mu_s \int_{4\pi} L(r,t,\hat{s})P(\hat{s},\hat{s}')d\Omega' + S(r,t,\hat{s}) \qquad (1.9)$$

where *L(r,t,s)* is the radiance in the medium (units of W/m²sr) as a function of position r in the direction defined by unit vector $\hat{s}$. The RTE is a balance equation describing the conservation of energy within a medium. Other parameters include the velocity of light in the medium, v, the scattering phase function, P ($\hat{s}$,$\hat{s}$'), the source term, S (r,$\hat{s}$,t) representing power injected into a unit volume, and the solid angle around $\hat{s}$. This equation has been used to describe processes in nuclear physics, oceanography, astrophysics and as of the 1990s for biomedical optics applications as well[15]. Unfortunately, because of the complexity of the RTE, it has no general analytical solutions and must be solved by numerical methods.

1.3.1   The Diffusion Approximation

The RTE can be greatly simplified by the diffusion approximation for media where the radiance can be assumed nearly isotropic (which is satisfied by replacing μ_s with μ'_s),

scattering events greatly out number absorbing ($\mu'_s \gg \mu_a$), and the source-detector distance is relatively large. These assumptions are valid for biological tissues if the volume being interrogated is large enough such that photons are scattered multiple times and lose all sense of direction. Mathematically the diffusion approximation for light transport is simple and can be expressed in the following form:

$$\left(\frac{1}{v}\frac{\delta}{\delta t} - D\nabla^2 + \mu_a\right)\Phi(r,t) = S(r,t) \tag{1.10}$$

Where Φ is the fluence and D is the diffusion constant:

$$D \equiv \frac{1}{3(1-g)\mu_s + \mu_a} \equiv \frac{1}{3[\mu'_s + \mu_a]} \tag{1.11}$$

Analytical solutions are available for defined geometries and boundary conditions. For these solutions, the source is assumed to be an isotropic point and the scattering isotropic within the medium, simplifying the phase function to a constant factor. Assuming the source can be represented by an infinitesimal short pulse of light, the time-dependent solution to the diffusion approximation for an infinite medium is given by[30]:

$$\Phi(r,t) = v(4\pi Dt)^{-\frac{3}{2}}exp(\mu_a vt)exp(\frac{-r^2}{4\pi Dt}) \tag{1.12}$$

1.4   In-vivo Spectroscopy

The various NIRS techniques can be divided based on differences in the light source and detectors implemented. The most commonly used techniques will be described in this section. In general, all approaches aim to generate quantitative measurements of chromophore concentrations by delineating absorption and scattering effects. To do this, these methods consider changes in light intensity, in conjunction with another dimension (location, time, frequency, wavelength) to get a complete picture of the light propagation resulting from its optical properties.

1.4.1 Continuous Wave (CW) NIRS

The most basic NIRS system employs continuous-wave sources at two or more wavelengths that target the changes in absorption due to HHb and HbO_2, and only changes in light intensity are measured using photodiodes. These CW systems are inexpensive and can be reduced to small wireless devices[31,32]. However, this approach only allows for quantification of relative measures of hemoglobin concentration or StO_2 because it does not provide enough information to determine the optical properties of tissue or the differential pathlength of the light. In some situations, relative measures may be adequate if one is looking at changes due to treatment for example. However, quantitative measurements are required when making judgments between patients or setting treatment thresholds[33].

1.4.1.1 Spatially resolved NIRS

Spatially resolved spectroscopy (SRS) is a modification of CW-NIRS that attempts to provide quantitative measures by acquiring light attenuation at multiple source-detector distances. This technique was first demonstrated by Matcher et al. and is the technology behind many commercial systems[34].
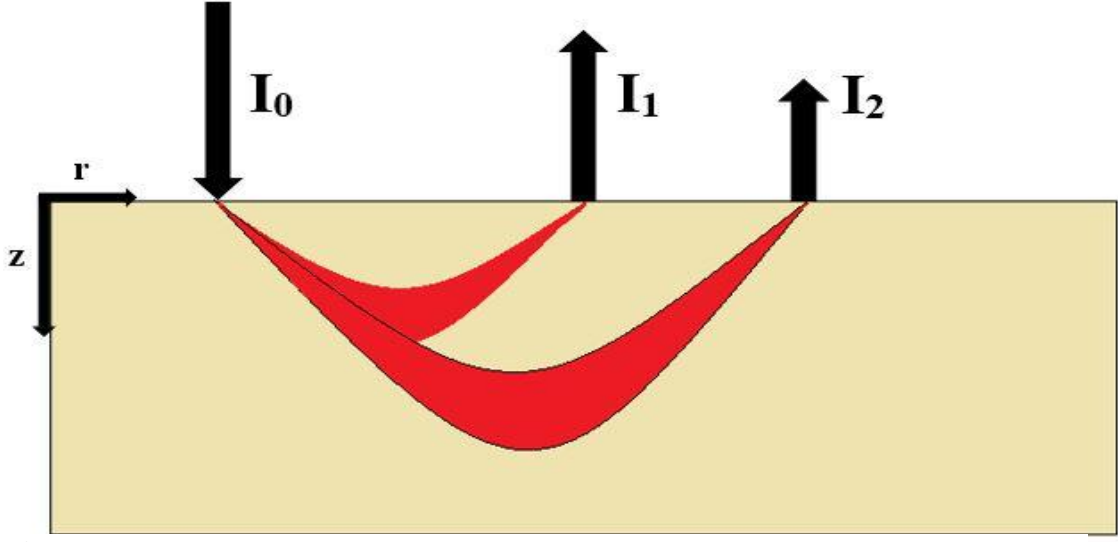
Figure 1-2 Schematic Diagram of Spatially Resolved NIRS

 If we consider a homogeneous semi-infinite medium with a collimated light source incident at the surface ($z = 0$) at $r = 0$ and a detector at $r = r_{sd}$, then the diffuse reflectance as a function of the source detector distance, $R(r_{sd})$ is given by[34]:

$$R(r_{sd}) = \frac{z_0}{2\pi} \frac{exp\left[-\mu_{eff}(z_0^2 + r_{sd}^2)^{\frac{1}{2}}\right]}{z_0^2 + r_{sd}^2} \left[\mu_{eff} + \frac{1}{(z_0^2 + r_{sd}^2)^{\frac{1}{2}}}\right], \qquad (1.13)$$

where z_0 ($1/\mu'_s$) is the depth where the incident light can be considered isotropic and has entered the diffusive regime. The effective attenuation, μ_{eff}, is defined as

$$\mu_{eff} \equiv \sqrt{3\mu_a(\mu_a + \mu'_s)} \approx \sqrt{3\mu_a\mu'_s}, \qquad (1.14)$$

since $\mu'_s \gg \mu_a$. When r_{sd} is large, ($r_{sd} \gg z_0$ and μ_{eff}), which is true for commercial NIRS devices that employ a source-detector separation of 3 to 4 cm, the equation for the diffuse reflectance can be simplified, and the natural logarithm yields a linear relationship with $-\mu_{eff}$ as the slope as follows:

$$ln[r_{sd}^2 R_d(r_{sd})] = -\mu_{eff} r_{sd} + intercept. \qquad (1.15)$$

Therefore, by plotting $ln[r_{sd}^2 R_d(r_{sd})]$ versus r_{sd}, for at least two source-detector separations, an estimate of μ_{eff} can be extracted. Since μ_{eff} is a function of both μ_a and μ'_s to measure each independently requires more information. On commercial systems, μ'_s is set to assumed values in order to extract μ_a and ultimately the hemoglobin concentrations[35].

Commercial devices that use SRS have been compared in a number of studies and there have are strong correlations between approved devices. This is expected as they are attempting to measure the same quantities, however, there are consistent differences between absolute values of StO_2[18,19,36]. These differences may be a result of differences between in-vivo calibration or scaling methods. Regardless of the reason, differences between measurements suggest that these systems are more suited for trend monitoring. The ultimate objective of NIRS measurements is to obtain direct, non-invasive measure of cerebral oxygenation, so that events such as hypoxia, ischemia or hyperoxia can be detected, evaluated and acted upon. For this to happen, NIRS StO_2 measurements need to be reliable and reproducible. Otherwise, it becomes difficult to define normal ranges and thresholds for intervention when different clinically used devices yield different readings.

1.4.2   Time-Resolved NIRS

Time-resolved (TR)-NIRS was first introduced in 1988 by Chance et al and Delpy et al.[37,38]. This technique relies on extremely short pulses of light, of the order of a few picoseconds in duration, emitted from a laser source. Sensitive detectors with high temporal resolution generate a histogram of the number of photons detected and their arrival times, which are referred to as temporal point spread functions (TPSF). These time-sensitive components allow for quantitation because DP can be obtained from the mean time of flight of photons from the generated histogram. Additionally, the optical

properties (μ_a, μ'_s) can be extracted by modeling the TPSF by the diffusion approximation. The time dependent solution for a semi-infinite geometry is given by the following equation[39]:

$$R_d(r_{sd}, t) = \frac{1}{2}(4\pi Dc)^{-\frac{3}{2}}t^{-\frac{5}{2}}e^{(-\mu_a ct)}\left[z_0 e^{-\frac{r_1^2}{4Dct}} + (z_0 + 2z_b)e^{-\frac{r_2^2}{4Dct}}\right] \quad (1.86)$$

Where, $r_1^2 = z_0^2 + r_{sd}^2$ and $r_2^2 = (z_0 + 2z_b)^2$. With quantitative measurements of optical pathlengths and tissue optical properties, chromophore concentrations can be derived, along with StO₂. A drawback of this technique is that the fast firing lasers, sensitive detectors and timing controls that are required are more expensive and technically complex, which has hampered clinical translation.

A conceptually similar approach to TR-NIRS is frequency domain (FD) NIRS, which modulates the emission light intensity at a known frequency and collects intensity and phase data, as opposed to time-encoded measurements. Typically, the light intensity is modulated at a single frequency (100 MHz) so the FD-NIRS is not completely analogous to TR-NIRS. However, the change in the phase of the detected light is proportional to the mean optical pathlength. These systems are less complex than TR systems, but require calibration to be quantitative, and phase measurements are inherently noisy. Although a commercial FD-NIRS system is available (ISS Inc.), they are not used as commonly as CW-NIRS systems in the NICU.
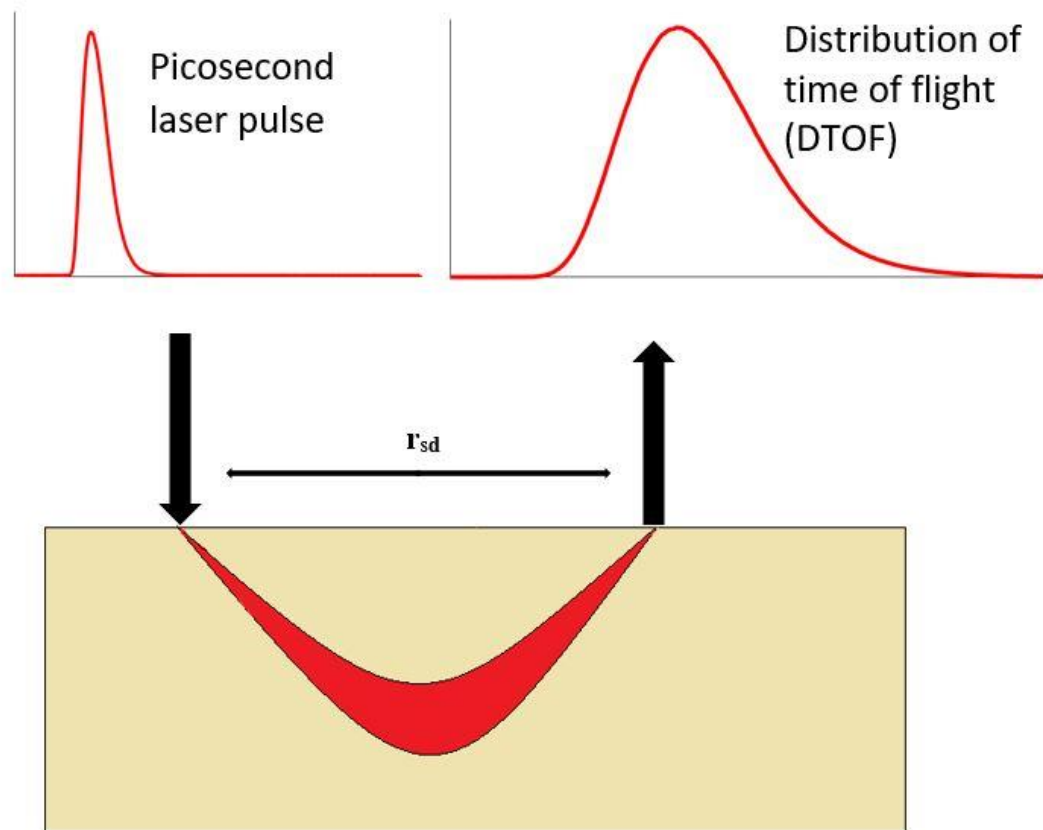
Figure 1-3: A depiction of an incident laser pulse to tissue and the resulting TPSF detected a distance away using a TR-NIRS system. Information regarding depth can be extracted by restricting analysis to early or late arriving photons, where late arriving photons will have a larger optical path length and will be more sensitive to deeper tissues.

1.4.3   Derivative Spectroscopy

A final NIRS approach for separating scattering and absorption effects is derivative spectroscopy, which was first proposed by Matcher et al.[29]. This approach is based on acquiring attenuation data across the entire NIR spectrum, which is accomplished using a white light source and a spectrometer to detect reflected light intensity as a function of wavelength. Given the fact that scattering is only weakly dependent on wavelength, its

influence on measured attenuation spectra can be removed by generating the second derivative. In terms of the modified Beer-Lambert law, DP can be considered wavelength independent over a small range and the scattering term, G(λ), in Eqn 1.7 will become negligible in the second derivative spectrum. Only a relationship between attenuation and chromophore concentrations is left in the second derivative of the modified Beer-Lambert law:

$$\frac{\partial^2 A(\lambda)}{\partial \lambda^2} = DP \sum_i \frac{\partial^2 \varepsilon_i(\lambda)}{\partial \lambda^2} C_i \tag{1.17}$$

In order to quantify chromophore concentrations, DP must be determined, which can be done by assuming a known concentration of water. In the brain, the water concentration is quite stable at approximately 85%[40]. With the DP determined, the HHb concentration can be determined by its second derivative feature centred around 760 nm. Derivative spectroscopy has the advantage of removing DC effects that may be cause by imperfect coupling between fibers and tissue and therefore does not rely on a calibration step like FD-NIRS. However, the concentration of HbO_2 cannot be reliably determined because it does not have any unique features in the second derivative of its spectral absorption.
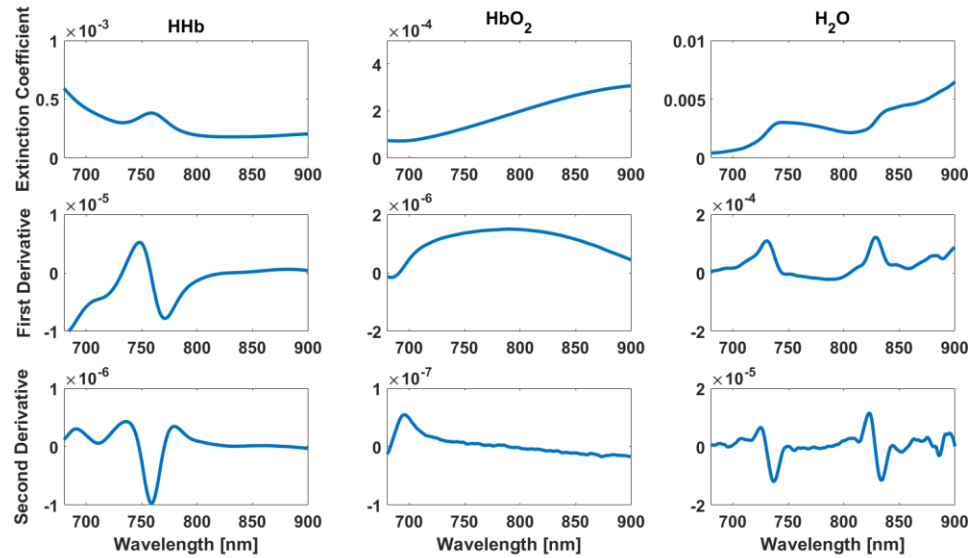
Figure 1-4 Extinction coefficients of endogenous chromophores and their corresponding first and second derivatives in the rows below. (units are g/dl/mm for hemoglobin and %/mm for water)

This method has been expanded in order to fit for the water concentration instead of assuming a known value, as well as by extending the analysis to include the first derivative spectrum in order to fit for the concentration of HbO_2[41–43]. This procedure requires modeling light propagation by the diffusion approximation rather than using the Modified Beer Lambert law. The steady-state solution for the reflectance in a semi-infinite, turbid medium is[39]:

$$R(r) = \frac{1}{4\pi}\left[z_0\left(\mu_{eff} + \frac{1}{r_1}\right)\right]\frac{e^{(-\mu_{eff}r_1)}}{r_1^2} + (z_0$$
$$+ 2z_b)\left(\mu_{eff} + \frac{1}{r_2}\right)\frac{e^{(-\mu_{eff}r_2)}}{r_2^2} \tag{1.98}$$

With this approach, the wavelength dependence of scattering is modeled by equation 1.6, is incorporated into the analysis of the first derivative spectrum. By determining both HbO_2 and HHb, oxygenation saturation can be derived.

The developed derivative spectroscopy method has been used to determine the optical properties of a two-layered phantom modeling an adult head. By incorporating multiple distance measurements, the optical properties of the lower "brain" layer were determined within reasonable accuracy.[44] In another work, the HHb concentration and water fraction derived using the diffusion approximation were in good agreement to values obtained by applying the MBLL to second derivative spectra. [42]. One of the major advantages of this technique is the fact that the equipment is inexpensive (figure 4). Even a small off-the-shelf spectrometer was found to be adequate with minor modifications[41]. Derivative spectroscopy has been used alongside another optical technology, diffuse correlation spectroscopy (DCS), to measure changes in StO_2 as well as CBF in neonates with patent

ductus arteriosus undergoing treatment[40]. Recently, derivative spectroscopy was also used in the NICU to investigate changes in blood flow and oxygen and metabolism in preterm infants undergoing treatment for PHVD [43]. Finally, this hyperspectral NIRS (H-NIRS) approach was recently combined with DCS to provide continuous monitoring of cerebral blood flow, StO_2 and CCO in a piglet model of hypoxic-ischemia[45]. These studies show the capabilities of this relatively simple optical technology; however, there has not been no study aimed at validating the StO_2 measurements derived by this method.
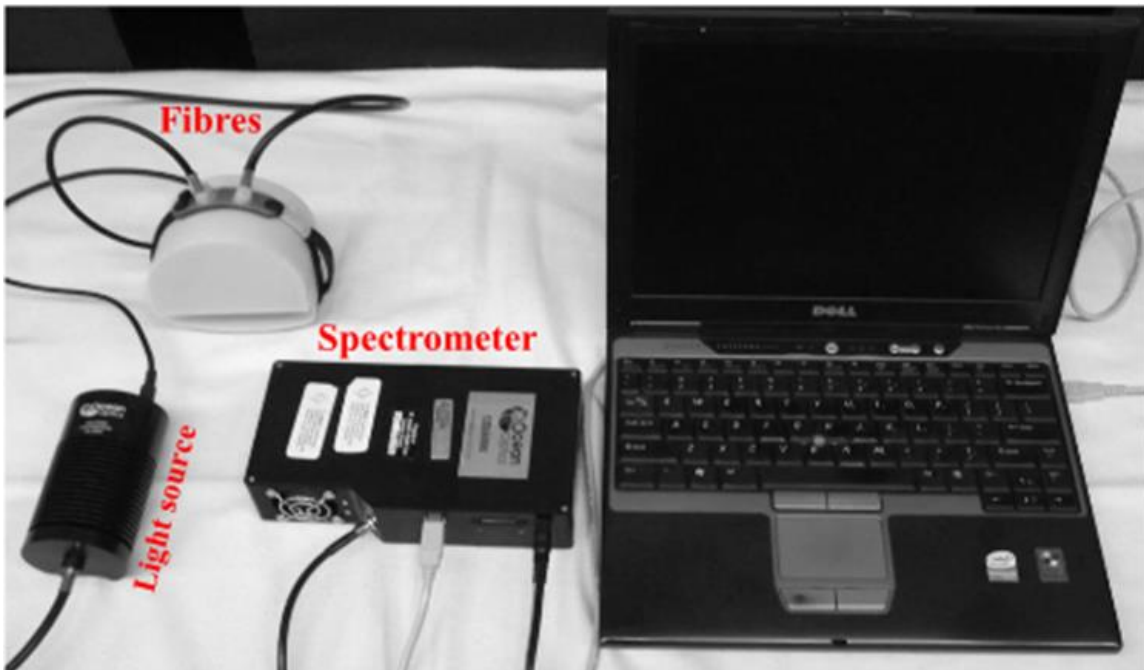
Figure 1-5 Simplistic hyperspectral NIRS set up

1.5   Research Objectives

Preterm infants in the NICU are vulnerable to brain injuries that can result in lifelong disabilities. Because of this, there is a growing recognition of the need for reliable brain monitoring techniques to help guide clinical management. NIRS has long been considered ideal for this purpose, and clinical trials are beginning to demonstrate the

potential of NIRS, despite the limitations of current commercial systems. More advanced technologies, such as TR-NIRS, can provide quantitative measurements, but clinical translation will likely continue to be hindered by practical issues related to cost and complexity of the systems. Hyperspectral derivative spectroscopy offers an inexpensive alternative that has been shown in preliminary clinical studies to be sensitive to cerebral oxygenation changes. Furthermore, it is the only NIRS method capable of also reliably monitoring CCO[45,46].

The objective of this work was to validate StO_2 measurements obtained by derivative H-NIRS to independent measurements obtained by TR-NIRS, which is considered the gold standard for quantifying tissue optical properties. A piglet model of hypoxia was used to compare StO_2 measurements by the two systems, where multiple levels of oxygenation were explored for each animal. Steady-state measurements were made by both systems at each oxygenation state so that comparisons could be made between measures of the optical properties, μ_a and μ'_s , the chromophore concentrations, HHb and HbO_2, and most importantly StO_2. In addition to assessing the accuracy of H-NIRS, the precision of the StO_2 measurements was investigated by assessing the with-in subject variability at baseline oxygenation levels and compared to commercial devices in literature. These fundamental measurements are extremely pertinent for translating this technology to the clinic[24].

Chapter 2

2   Materials and Methods

2.1   Animal Preparation

Animal experiments were conducted in accordance with the guidelines of the Canadian Council of Animal Care (CCAC) and approved by the Animal Care Committee at Western University. Newborn piglets were obtained from a local supplier on the day of the experiment. Following anesthetic induction with 5% isoflurane, anesthetic was reduced to 3% for surgical procedures, and maintained at 2-2.5% isoflurane. Animals were tracheotomized and mechanically ventilated on a mixture of 2 L oxygen and 2 L medical air. Vital signs including heart rate (HR), arterial O_2 saturation (SaO_2), CO_2, respiratory rate and temperature were monitored (SurgiVet, Smith Medical, MN) as well as invasive blood pressure via a femoral artery catheter. Arterial blood samples were also collected via the femoral catheter for blood gas and glucose analysis (Radiometer, ABL 80 FLEX CO-OX, Denmark). Lateral ear and cephalic veins were catheterized for IV access and infusion of NaCl fluids (4 ml/kg/h) for the duration of the study. The top of the head was shaved, and the piglet was placed in prone position in a plexiglass jig to help support a 3D printed probe holder fastened to the head which held the NIRS probes.

Figure 2-1 Set-up showing position of the optodes on the head of a newborn pig.

2.2   Experimental Procedure

Prior to each experiment, the TR-NIRS system was allowed 1 hour to warm up in order for the lasers to stabilize[47]. Additionally, the spectrometer for the H-NIRS system was calibrated using a neon light source with known spectral features contained in a light opaque box.

After the animal was prepped, an arterial blood sample was taken to measure baseline arterial partial pressure of oxygen (PaO_2). TR-NIRS measurements consisted of two sets of data, each consisting of 256 averages acquired over 86 s. Within each data set, TPSFs were acquired in sets of two wavelengths (670 and 804 nm followed by 760 and 830 nm). The lasers were pulsed at a repetition rate of 40 MHz to provide a time window large enough to avoid signal contamination between the two TPSFs. This was verified in a series of preliminary experiments (data not presented). A second blood draw was taken for gas analysis before the H-NIRS measurements to ensure PaO_2 remained stable between techniques. The H-NIRS measurement protocol consisted of collecting 256 spectra in a 64-s period.

The fraction of inspired oxygen (FiO_2) was subsequently reduced in steps by adjusting the combination of ventilated oxygen, medical air (21% O_2, remainder N_2), and N_2. Consistent FiO_2 levels were utilized across animals at 60.5, 41, 31, 26, 21 and 20%, while further reductions were applied for animals who had muted responses to the changes. After a new FiO_2 level was established, the change in PaO_2 was used to determine if NIRS acquisitions or further inspired gas adjustments were needed. At each of these steps, 3-5 min was allotted to allow for the displayed heart rate, blood pressure and SpO_2 readings to reach a steady state before acquiring blood gas and NIRS measurements. Each experiment was comprised of seven to ten oxygenation stages ranging from hyperoxia to hypoxia. The lower hypoxic limit was determined by the PaO_2 measurement < 40 mmHg at which the piglet vitals remained stable.

After the hypoxia challenges were completed, a H-NIRS reference spectrum was acquired and the TR-NIRS IRFs were measured as described below.

2.3 NIRS Instrumentation

2.3.1 Hyperspectral System

The H-NIRS system utilized a 20 W halogen lamp light source (Ocean Optics HI-200-HP), and its output was directed to the tissue by an optical fiber bundle (3.5 mm active diameter, 30 µm core, 0.55 numerical aperture). Diffusely reflected light was collected from the scalp by another fiber bundle (3.85 mm active diameter, 50 µm core, 0.22 numerical aperture) at a distance of 3 cm from the emission fiber bundle and directed to a custom-made spectrometer (P&P Optica, ON, Canada), coupled to a CCD Camera (Andor iDUS 420 BEX2-DD, Oxford Instruments). The spectrometer used a 1024 x 256 pixel CCD and had a spectral range of 548 - 1085 nm with a 1.65 nm resolution. It was operated at a temperature of -80 °C with a 250 ms exposure time.

Reference spectra were acquired by placing the emission and detection probes at either end of a 26.5 cm light-tight box. The iris on the halogen lamp was adjusted to reduce to avoid saturating the CCD camera.
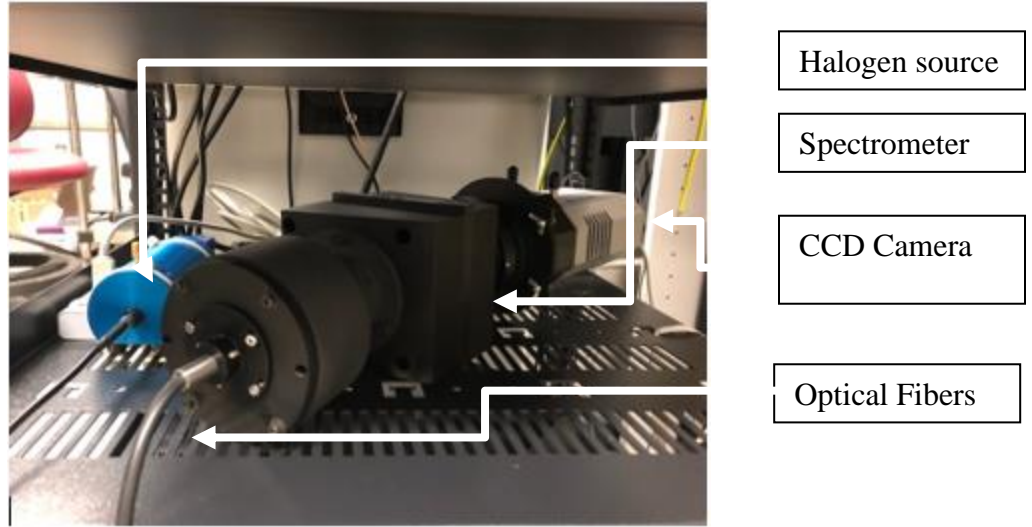
Figure 2-2 Main Hyperspectral NIRS components: broadband source and spectrometer

2.3.2   Time-Resolved System

The in-house-developed TR-NIRS system consisted of picosecond pulsed diode lasers operating at wavelengths of 670, 760, 804 and 830 nm (PicoQuant, Germany) and a repetition rate of 40 MHz using a computer-controlled laser driver (PDL 828, PicoQuant). These lasers were coupled to two bifurcated fibers ($\varphi = 0.4$ mm, NA = 0.22, Fiberoptics Technology, CT, United States), which directed light to the piglet's head. Diffusely reflected light was collected from the tissue surface by a fiber bundle ($\varphi = 3.6$ mm, NA = 0.55, Fiberoptics Technology) that was 3 cm from the emission fiber and delivered to hybrid photomultiplier tubes (PMA Hybrid 50, PicoQuant). A HydraHarp 400 (PicoQuant) time-correlated singe-photon counting unit was used to record the arrival times of the photons and DTOFs were assembled using LabView Software (National Instruments, TX, United States).

An impulse response function (IRF) was acquired for each wavelength using a 6 cm PVC box that contained a neutral density filter (Thor Labs, NJ, United States) to reduce laser

intensity as well as white paper to disperse the light beam. The incorporation of the IRFs in the data processing is discussed in the next section.
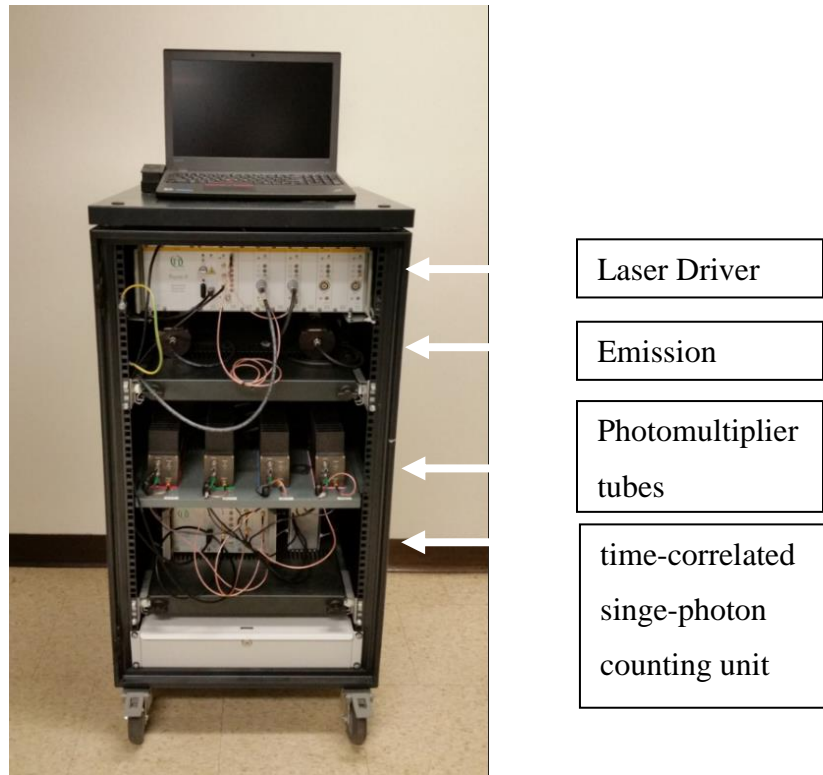
Figure 2-3 TR-NIRS system housed in a portable cart

2.4   Data Analysis

Light transportation through a piglet head was modeled by the solution to the diffusion approximation for a semi-infinite medium. This solution was considered acceptable because signal contamination from the extra-cerebral layer would be small at a source-detector separation of 3 cm due to a relatively thin scalp and skull[48]. The absorption coefficient was defined as a sum of the three main endogenous chromophores: HHb, HbO_2, and water:

$$\mu_a(\lambda) \ = \ [HbO_2] \cdot \varepsilon_{HbO_2}(\lambda) \ + \ [HHb] \cdot \varepsilon_{HHb}(\lambda) \ + \ WF \cdot \varepsilon_{H_2O}(\lambda) \qquad (2.1)$$

where $\varepsilon_i(\lambda)$ represents the molar extinction coefficient of the ith chromophore and WF is the water fraction in tissue. The wavelength dependency of μ_s' was modelled by:

$$\mu'_s(\lambda) = \beta \left(\frac{\lambda}{800}\right)^{-\alpha} \qquad (2.2)$$

where β is the value of μ'_s at 800 nm and α characterizes the expected reduction in scattering with increasing wavelength.

Spectral analysis began by applying a wavelet de-noising algorithm that first transformed Poisson noise to Gaussian noise using the Anscombe transformation on the acquired spectra. This Gaussian noise was then removed by wavelet de-noising, and applying the inverse Anscombe transformation to obtain a noise-reduced spectra[49]. Smoothing was performed using a 5-point moving average filter before generating derivative spectra to minimize noise contributions. Chromophore concentrations and the scattering terms were determined in a series of steps involving fitting the solution to the numerical derivatives to the diffusion approximation to the derivative spectra (figure 2-4). First, the WF was determined by fitting the water feature between 815 and 840 nm in the second derivative spectrum. With WF determined, the HHb concentration was determined by fitting the second derivative spectrum between 690 to 775 nm to capture the characteristic HHb feature centered at 760 nm. With these two parameters fixed, the model was fit to the first derivative spectrum to determine the HbO$_2$ concentration and the scattering terms β and α. The fitting range was between 690 to 840 nm. Fitting was performed using a constrained optimization routine based on the MATLAB script fminsearchbnd with upper and lower boundaries set to span published values[41].

The scattering terms as well as the water fraction were included as fitting parameters in the analysis of the first spectrum at hyperoxia (60 % O$_2$) and these values were fixed in

the analysis of all subsequent spectra. At each level of oxygen, the estimates of [HbO₂] and [HHb] from the spectra analysis were used to calculate StO₂ according to:

$$StO_2 = \frac{[HbO_2]}{[HbO_2] + [HHb]} \qquad (2.2)$$
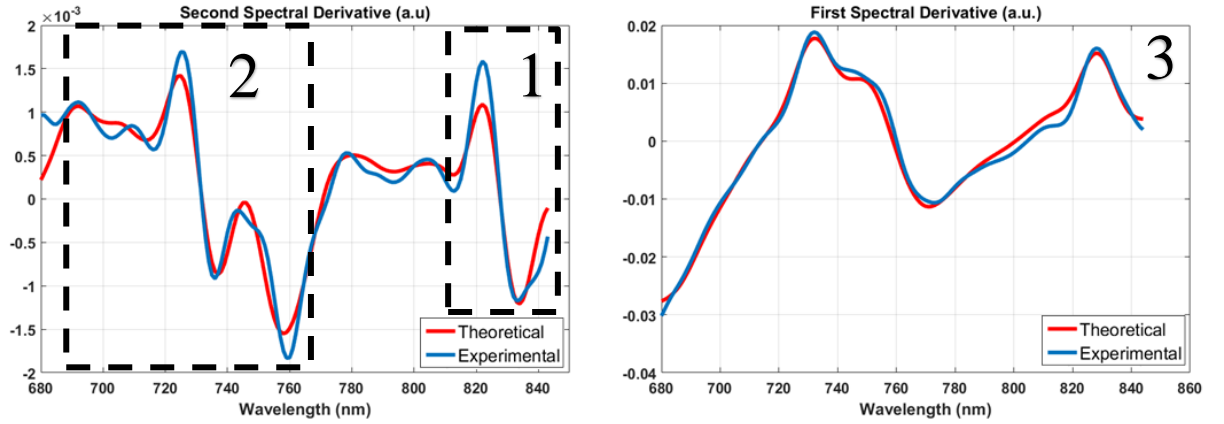
Figure 2-4 Best fit of the diffusion approximation to measured derivative spectra in the following order: (1) water fit to second derivative spectra, (2) [HHb] fit to the second derivative spectra, and finally (3) [HbO₂], β and α derived from fit of first derivative spectrum.

The TR-NIRS data were analyzed using the time dependent solution to the diffusion approximation for a semi-infinite medium[39]. The first step was to convolve the model solution with the measured IRF to correct for temporal dispersion caused by the system. Each IRF was temporally adjusted to account for size of the response box. Next, the model was fit to the acquired TPSFs using three parameters: μ_a and μ'_s, and an amplitude factor that accounts for laser power, detection gain and coupling efficiency[50]. Fitting was performed using an optimization routine based on the MATLAB script fminsearch. The fitting range was set to 80 % of the peak value on the ascending edge and 20 % on the descending edge of the TPSF. After the fitting of the baseline data, μ'_s and the amplitude factor were fixed for the remainder of the measurements. Maintaining the same technical

set-up throughout all experiments ensured that the amplitude term did not change, and it has been showed that μ_s' does not change unless under extreme circumstances like asphyxia or death[51,52].
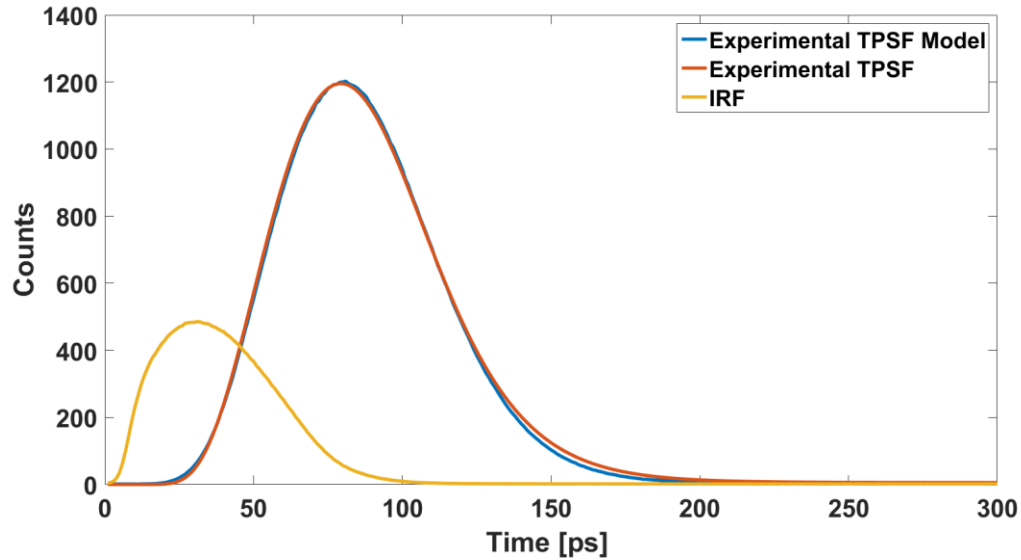
Figure 2-5 Experimental TPSF and IRF with the best-fit of the diffusion approximation.

2.5 Statistical Analysis

SPSS 25 (IBM, NY, United States) was used for all statistical analyses. Interactions between the two NIRS techniques of measuring StO_2 at different FiO_2 levels were investigated by a two-factor repeated-measures ANOVA with the level of FiO_2 and the different measurement techniques are the factors. A straightforward statistical test could not be used to determine significance of correlations between the two sets of StO_2 measurements because multiple measurements were collected from each animal. Instead, a variation of the generalized estimating equation technique was utilized. First, a linear fit was applied to the data from each piglet individually. Second, a significant correlation was tested by using a t-test to compare the average of the distribution of slopes against the null hypothesis (i.e., slope = 0). Finally, the distribution of slopes was compared with

a slope of 1 to determine the agreement with the line of identity. A linear mixed effects model was used to evaluate the inter-subject variability of StO_2 with StO_2 as the random variable and subject as a factor. To measure the within-subject variability the first three measurements, prior to noticeable change in oxygenation, were grouped and used in the same mixed model analysis. All group average values in the experiment are presented as means $\pm$ SD and statistical significance was defined as $P < 0.05$.

Chapter 3

3 Results

3.1 Physiological Parameters

Eight piglets (4 female) were studied with an average of age of 4.4 +/- 2.3 days and an average weight of 2.3 +/- 0.7 kg. Each animal experienced 7 to 10 levels of oxygenation. Table 1 presents a summary of the physiological parameters at six FiO_2 steps that were experienced by all animals. As expected, both SaO_2 and arterial PaO_2 dropped significantly as FiO_2 was reduced. No statistically significant differences across the different FiO_2 values were found for arterial PCO_2, arterial blood pressure, and temperature. However, heart rate rose significantly at the most extreme hypoxic condition. In total, 68 sets of TR-NIRS and H-NIRS measurements were completed.

Fraction of Inspired Oxygen, %	60.5	41	31	26	21	20
Arterial oxygen saturation, %	100	100 ± 0.3	99 ± 1.7	97 ± 3	$88 \pm 10*$	$74 \pm 12 *$
Arterial PO$_2$, mmHg	264 ± 29	$158 \pm 33*$	$111 \pm 24*$	$85 \pm 15*$	$57 \pm 13*$	$48 \pm 14 *$
Arterial PCO$_2$, mmHg	38 ± 3	40 ± 1	39 ± 1	46 ± 2	40 ± 1	40 ± 1
Mean Arterial Blood Pressure, mmHg	46 ± 4	47 ± 4	46 ± 4	45 ± 2	45 ± 3	46 ± 2
Heart rate, bpm	147 ± 12	151 ± 12	154 ± 14	157 ± 14	166 ± 17	$187 \pm 25 *$

Table 3-1 Clinical parameters of 8 piglets over 6 common FiO_2 levels. Values are means ± standard deviation. * P < 0.05 compared with corresponding 60.5% FIO_2 value.

3.2 Optical properties

Table 3-2 displays the baseline μ'_s values measured by H-NIRS and TR-NIRS. The TR values were extracted directly as a fitting parameter, while the broadband values were generated from the fitting parameters β and α. A significant difference between μ'_s values from the two techniques was found with the broadband values approximately half that of the TR values.

	670 nm	760 nm	804 nm	830 nm
TR μ'_s [cm^{-1}]	8.2 ± 0.1	7.4 ± 0.1	7.5 ± 0.1	7.1 ± 0.1
H μ'_s [cm^{-1}]	5.2 ± 0.1	3.9 ± 0.1	3.5 ± 0.1	3.3 ± 0.1

Table 3-2 Reduced scattering coefficient measured by the broadband and TR systems, compared at the four wavelengths acquired by TR-NIRS.

The mean *WF* value from the analysis of the baseline spectra was 85 ± 0.9%, which agreed with the assumed value of 85% used in the TR-NIRS analysis.

The wavelength dependency of μ_a as measured by H-NIRS is shown in figure 3-1 at three oxygenation levels. For comparison, each graph includes the corresponding μ_a measured by TR-NIRS at 4 discrete wavelengths. The level of agreement between the two methods appeared to improve as the oxygenation level decreased; however, there was not a significant effect between techniques determined by the repeated measures ANOVA ($F_{1,14}$ = 3.165 for 670 nm, 0.483 for 760 nm, 1.127 for 804 nm and 0.095 for 830 nm).
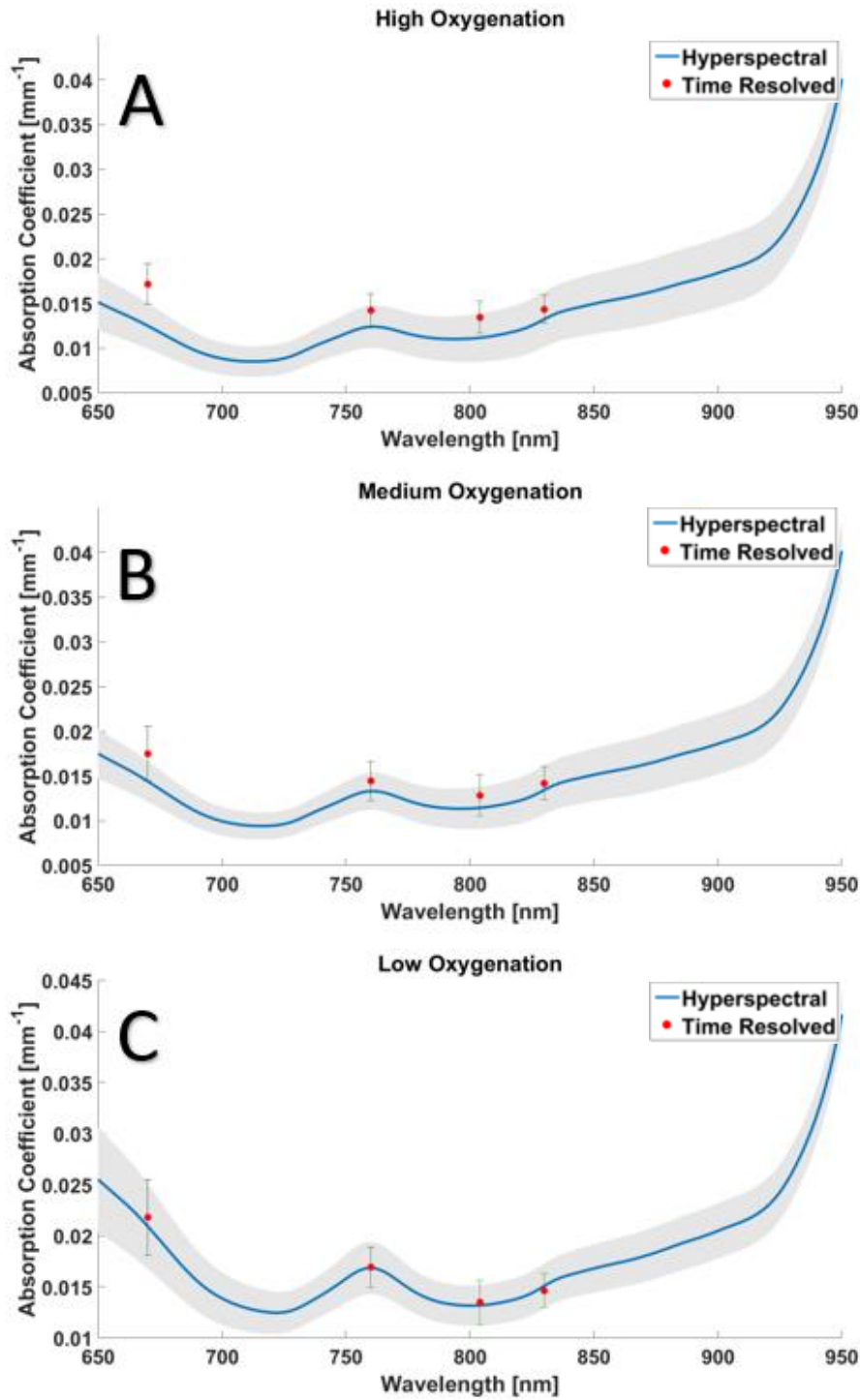
Figure 3-1 Absorption coefficients measured by H-NIRS (blue line, grey shadowing is the standard deviation) and TR-NIRS (red points, error bars are the standard deviation) across three levels of FiO_2 levels: (A) 60.5%, (B) 31% and (C) 20%.

3.3   Absorption Spectra

Figure 3-2 presents average absorption spectra measured by H-NIRS across eight piglets for three common FiO_2 levels, corresponding to 60.5%, 31% and 20%. Each spectrum was averaged over 256 repetitions (64 s). The corresponding average first and second derivatives of absorption are displayed in figure 3-3. An increasing amplitude corresponding to the 760 nm Hb feature was evident in the absorption spectrum and its derivatives as FiO_2 decreased. Additionally, there was no observable change in the water feature between 815 and 840 nm in the derivative spectra.
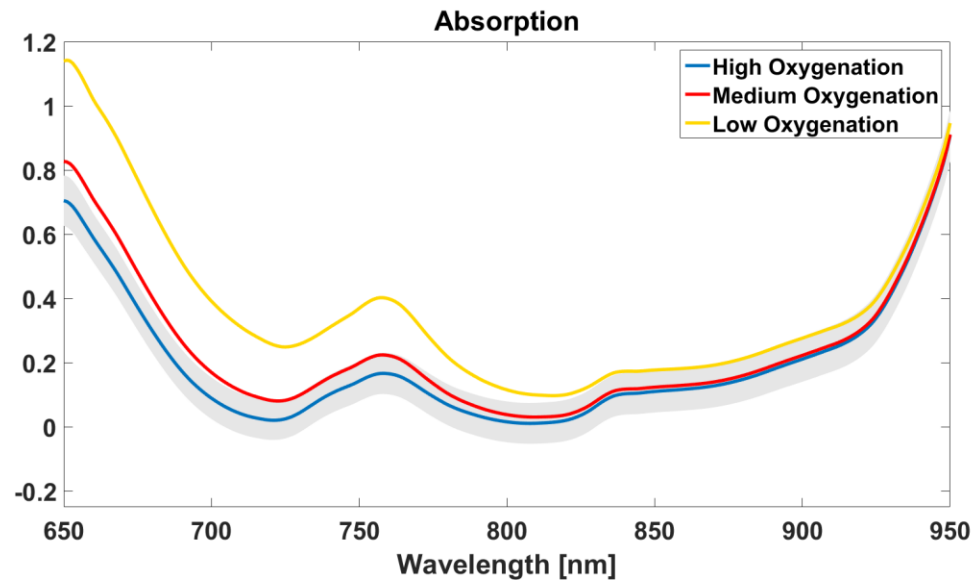
Figure 3-2 Averaged absorption spectra at three FiO_2 levels: 60.5% (high oxygenation), 31% (medium oxygenation) and 20% (low oxygenation). The standard error is presented for only the high oxygenation state for illustrative purposes.
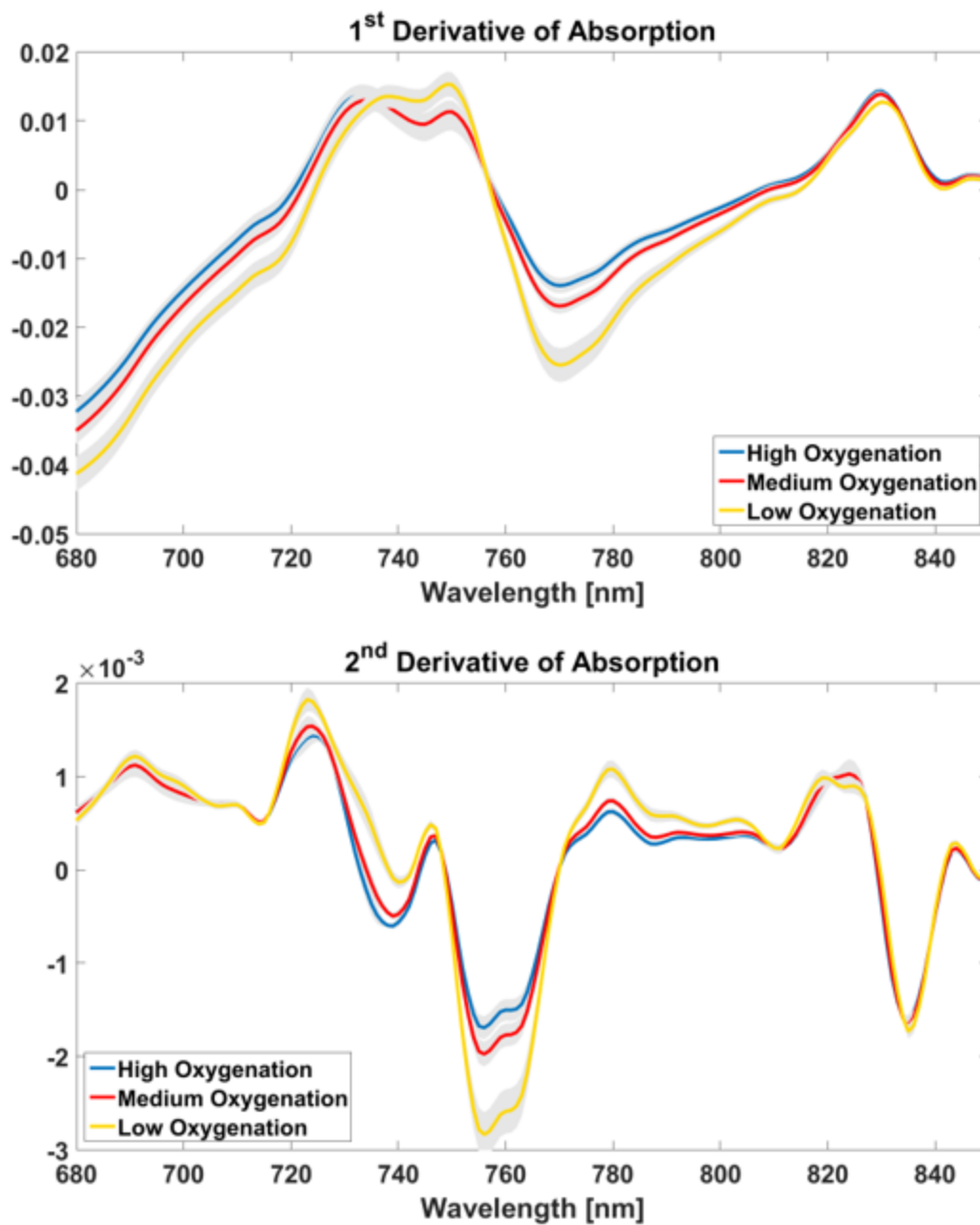
Figure 3-3 Averaged first and second derivative of absorption at three FiO_2 levels: 60.5% (high oxygenation), 31% (medium oxygenation) and 20% (low oxygenation). The grey shadowing represents the standard error of the averaged spectra.

3.4 Cerebral Oxygen Saturation

Measured cerebral oxygen saturation values from both the hyperspectral and TR-NIRS techniques are displayed in figure 3.4 as a function of arterial oxygen tension. Both NIRS techniques displayed the expected reduction in StO_2 with decreasing PaO_2. Repeated measures ANOVA revealed that there was no effect between the measurement techniques $(F_{5,35} = 1.591, p > 0.05)$.
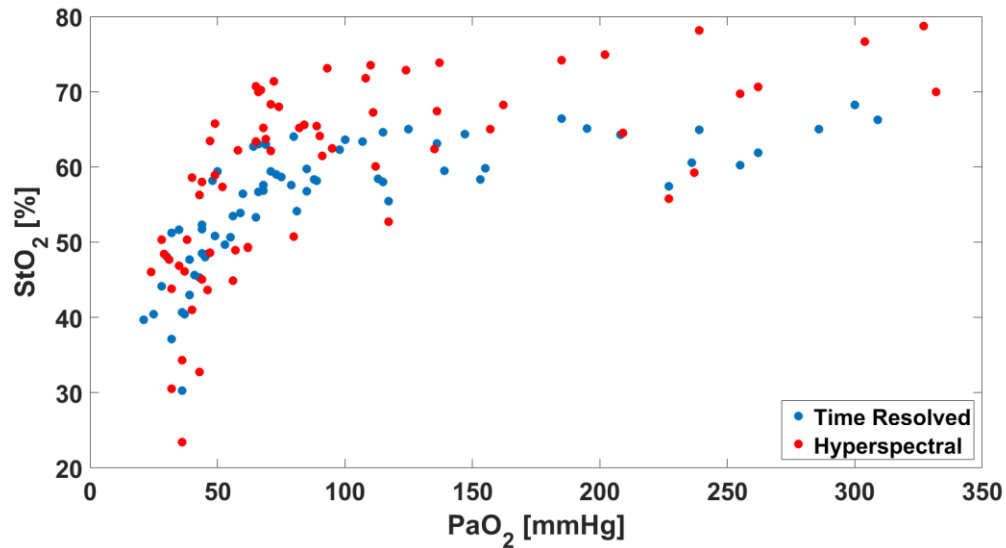
Figure 3-4 Relationship between cerebral oxygen saturation (ScO_2) measured by NIRS and arterial oxygen pressure (PaO_2).

Variability in StO_2 was characterized by the within-subject and between-subject coefficient of variation (COV) over the first three measurements where oxygenation was stable. The within-subject COV was 4% for H-NIRS and 2% TR-NIRS. The between-subject COV over the same oxygenation range was 11.4% for H-NIRS and 6.2 % for TR-NIRS.

The correlation between StO_2 measurements from TR-NIRS and H-NIRS is shown in figure 3.5. The top graph shows the results of the regression analysis for each individual animal. The lower graph depicts the data points from all animals and the average

regression line (slope = 1.38 ±0.3, intercept = -17.9 ±20.1% and R^2 = 0.95 ± 0.075). The average regression slope was significantly different from a slope of zero and the identity, while the intercept was also significantly different from zero. Bland-Altman analysis revealed an oxygenation level-dependent bias with mean differences and limits of agreement of -6.8 ± 11.2% at 60% FiO_2, -4.8 ± 9.5% at 31% FiO_2, and -4.4 ± 10.8% at 21% FiO_2. This bias was larger at the high StO_2 values, similar to the results of the regression analysis.

The correlations between the measured concentrations of oxy- and deoxyhemoglobin from the two NIRS techniques were explored in the same way as the StO_2 measurements displayed in figure 3-5. The regression slope, intercept and coefficient of determination were 1.25 ± 1.06, -11.9 ± 35.3, R^2 = 0.56 ± 0.27 for HbO_2 and 1.34 ± 0.49, -9.31 ± 7.8, R^2=0.96 ± 0.02 for Hb. The slopes for both chromophores were significantly different from zero and the identity, and the intercepts were significantly different from zero.
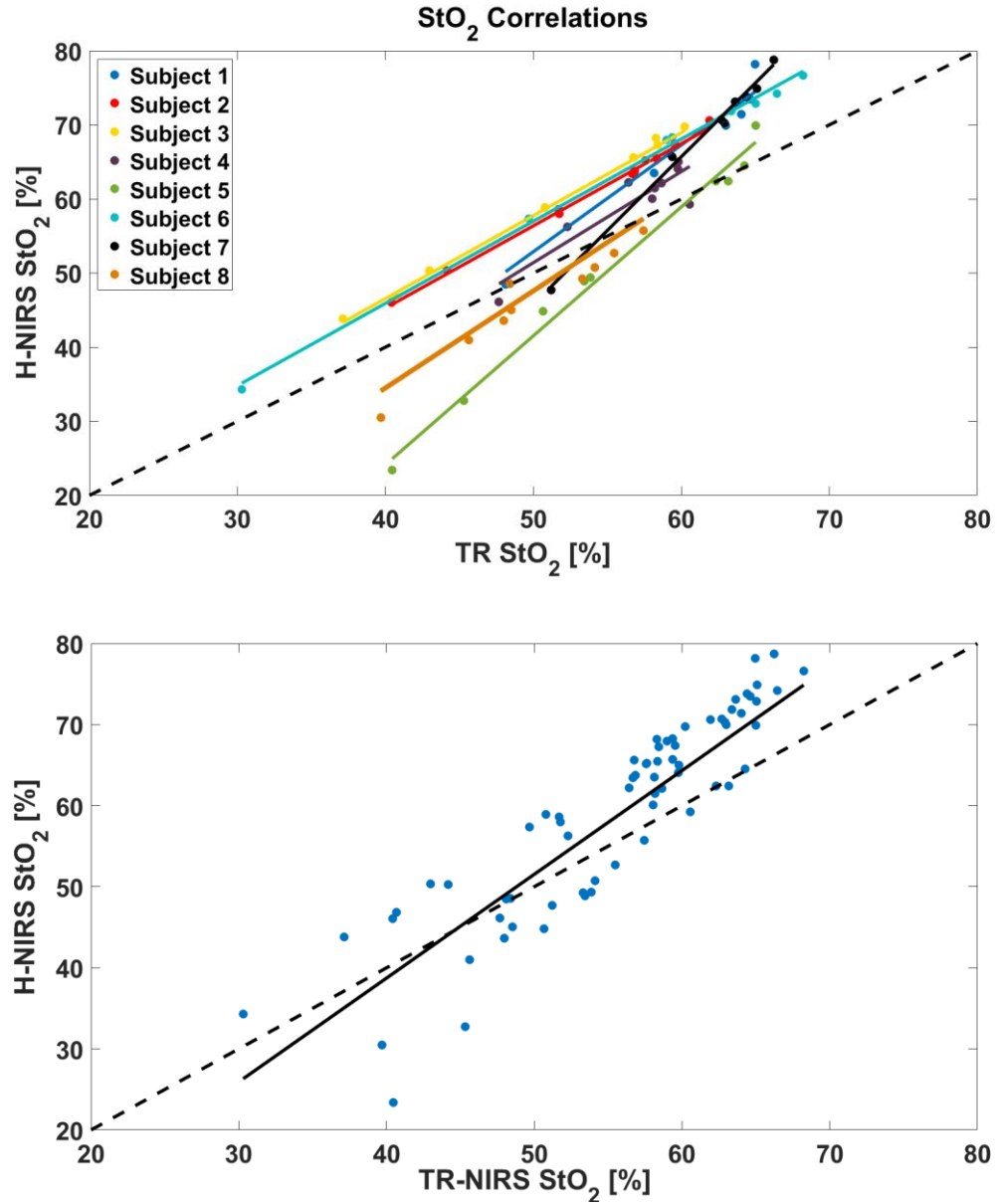
Figure 3-5 Top plot displays the regression between StO$_2$ measurements from TR-NIRS and H-NIRS for each individual animal. The bottom plot is the average regression across the 8 animals. There were 7-10 measurements per animal for a total of 68 data points. The dashed line represents the line of identity.
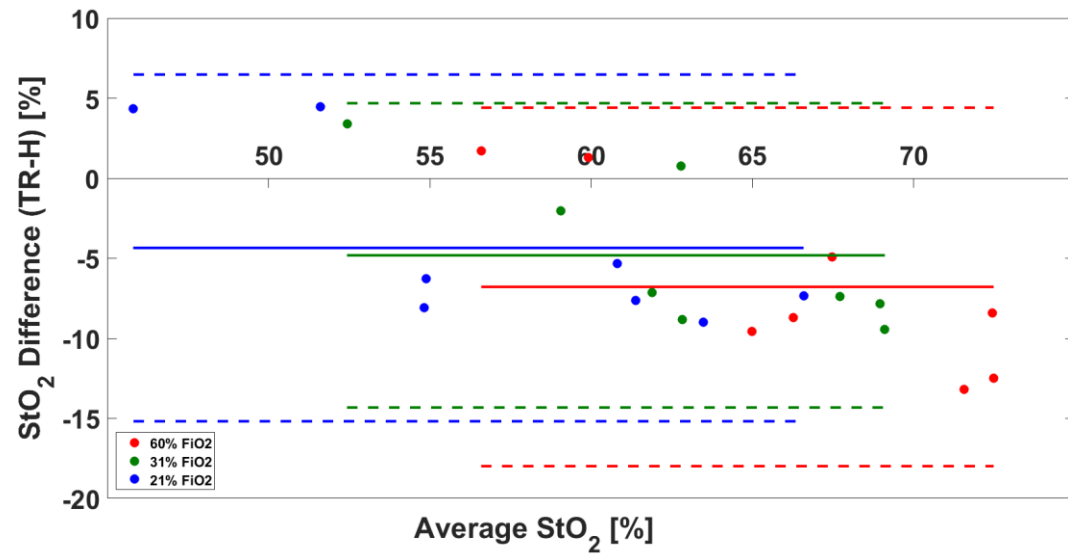
Figure 3-6 Bland Altman plot showing the differences in StO_2 from the two techniques. Each colour point represents a different FiO_2 level, the dashed lines indicate the limits of agreement and the solid lines are the mean differences between the techniques.

4 Discussion

NIRS is a tool that has shown promise as a monitor for cerebral health in preterm infants who are at risk of brain injury during the neonatal period. Clinical trials utilizing commercial NIRS system have shown that monitoring StO_2 can reduce the burden of hypoxia[53]. This study investigated the ability of a H-NIRS technique to measure StO_2. Using the whole NIR spectrum, instead of a few discrete wavelengths provides a means of quantifying chromophores in addition to oxy- and deoxy-hemoglobin. For instance, the exogenous blood flow tracer indocyanine green (ICG), which has a unique absorption spectrum, can be used with H-NIRS to measure CBF and the cerebral metabolic rate of oxygen ($CMRO_2$) by combining StO_2 and CBF[40]. Another example is cytochrome-c-oxidase which has a very broad absorption feature that can also be captured by H-NIRS and provides a continuous marker of oxygen metabolism[45]. Recently, H-NIRS was combined with DCS to provide continuous monitoring of CBF, StO_2, and CCO[45]. In this work the optical properties measured by H-NIRS were incorporated into the analysis of the DCS data to extract a marker of blood flow. Despite these applications, the accuracy of H-NIRS has not been rigorously tested. Therefore, the primary aim of this study was to assess the capability of H-NIRS as a cerebral oxygenation monitor. Experiments were conducted using a piglet model in which StO_2 could be measured over a wide range by creating different levels of hypoxia. For validation, StO_2 was measured by TR-NIRS since it is considered the gold standard NIRS approach for characterizing tissue optical properties.

The piglet model was chosen because newborn piglets are similar size to human infants, which enabled these experiments to be conducted with the same probes that could be used in clinical studies. Similar to neonates, signal contributions from the relatively thin extracerebral tissues are minimal. Alternatively, tissue-mimicking optical phantoms could have been used, as in previous comparison studies of NIRS oximeters[18] however, the set-

up is not trivial with regards to controlling oxygenation levels. In contrast, stable step changes in arterial oxygen saturation in the piglet model were achieved by manipulating the inspired mixture of gases, as evident by the SaO_2 and PaO_2 given in table 3-1. Despite differences in how individual animals responded in terms of changes in PaO_2, careful FiO_2 adjustments in each experiment could be performed in order to obtain StO_2 measurements over a wide range.

The main finding of this study was a strong correlation in StO_2 values from the two optical techniques. Across all experiments, the average coefficient of determination obtained from the comparison of H-NIRS and TR-NIRS StO_2 values was 0.95 ± 0.075 and the average regression slope was 1.38 ± 0.3, which was significantly different from the line of identity and from zero. A high coefficient of determination was found in each experiment, demonstrating a strong correlation between the two techniques, although the inter-subject variability was greater using the H-NIRS system. Additionally, the repeated measures ANOVA did not find a significant effect between the TR and H-NIRS measured StO_2 values. These results demonstrate that the H-NIRS method has the ability to measure StO_2 with comparable accuracy to the gold-standard technique.

Studies that have compared StO_2 measures from commercially available NIRS devices have shown similar degrees of correlation[18,19,36]. This is to be expected as devices designed to measure the same quantities should be highly correlated, so Bland-Altman analysis was used to determine the average difference between the techniques. Since multiple measurements were acquired from each animal, individual data points could not be treated as independent. To work around this issue, Bland-Altman tests were performed for each FiO_2 condition individually. Over the range of FiO_2 levels tested, the H-NIRS produced values that were 6.8 %, higher than the TR-NIRS measurements at 60 % oxygen and 4.4 % higher at 21% oxygen – all differences were significantly different from zero. In comparisons between commercial devices, differences between StO_2 values have ranged from 10 to 15% in studies involving preterm infants[19,54]. In the current study, the Bland-Altman analysis also uncovered an apparent oxygenation level-dependent bias: the overestimation of StO_2 by H-NIRS was larger at higher oxygenation levels.

In addition to investigating the agreement between StO_2 values, this study also investigated the agreement between the two NIRS techniques with respect to other scattering and absorption variables. To begin with, there was no statistical difference in μ_a values derived from spectral analysis using Eqn. 2.1 and from TR-NIRS at the four individual wavelengths, although this agreement appeared to improve with decreasing oxygen saturation (Figure 3-1). A good agreement was also found in the correlation analysis of HHb concentration measurements from the two methods ($R^2 = 0.96$, 1.34 ± 0.49). However, the agreement was considerably poorer for HbO_2. In this case, the average regression slope was 1.25 ± 1.06 with an $R^2 = 0.56 \pm 0.27$. However, the average baseline concentrations of oxy- and deoxyhemoglobin measured by H-NIRS (35 and 14 μM, respectively) were in good agreement with previously published values[52]. Finally, the comparison between μ'_s estimates demonstrated that H-NIRS consistently underestimated the TR-NIRS estimates by approximately 50%. This underestimation of μ'_s by H-NIRS was reported in a previous study[42].

It is interesting that the two parameters that showed the greatest inconsistently between systems (HbO_2 and μ'_s) were derived from the analysis of the first derivative spectra. This would suggest that crosstalk between these fitting parameters may have contributed to the mean higher regression slope when the two sets of StO_2 values were compared. as well as improving μ_a agreement at decreasing oxygenation levels. Considering that the HbO_2 concentration decreases with lower FiO_2, its influence on StO_2 would diminish. This could also explain the improvement in agreement between μ_a values observed in figure 3-1 at lower oxygenation levels. Potential crosstalk between HbO_2 and μ'_s could be investigated using tissue-mimicking phantoms with known optical properties and hemoglobin concentrations, as described in the literature[55]. Other possible solutions would be to combine the spectral measurements with another NIRS system (e.g., TR or FD) to measure μ'_s directly at one or more wavelengths, or perhaps acquire spectra at multiple source-detector distances. These solutions would add complexity to the overall design of the system, and it should be remembered that the accuracy of StO_2 was greater than the individual fitting parameters.

Beyond the accuracy of the H-NIRS StO_2 measurements, the precision of the measurements is important to assess clinical applicability of this technology. In this current study, the within- and between-subject variations were evaluated using the first three measurements during which PaO_2 remained stable. For H-NIRS, the within-subject and the between-subject COVs were 4% and 11.4% respectively, which were roughly double the values derived for TR-NIRS (2% and 6%). The greater variability with the H-NIRS method was likely a result of the greater number of fitting parameters used to analyze the spectral data compared to TR-NIRS approach. However, these COV values are within the range reported in clinical studies. For instance, Sorensen and Greisen reported within- and between-subject COVs of 5.2% and 6.9%, respectively, using a commercial NIRS system[24]. A direct comparison between the two studies is difficult considering Sorenson and Greisen acquired data from infants at steady-state FiO_2, whereas the current study involved anaesthetized piglets, which could explain the greater between-subject variability.

This study was conducted under the assumption that TR-NIRS provides accurate measurements of the tissue optical properties and StO_2. However, it is not without its own challenges. One of the main challenges is the need to accurately measure the instrument response function. In this current study, the IRF was measured using a light-tight black box of known geometry and a neutral density filter to prevent saturation of detectors. The temporal position of the IRF was accounted for by shifting the measured response by the calculated time for light to travel the length of the box. Another potential source of error is assuming a known water concentration in the fitting procedure. However, the assumed value (85%) agreed with the measured values from H-NIRS. Demel et al. also reported that assumptions of WF between 75 and 95 % did not result in substantial error in StO_2 measurements[56]. Another potential issue was that the TR-NIRS results did not show the wavelength dependency of μ'_s expected by a power law. This discrepancy may be due to the fact that the data were acquired in two sets and would likely be resolved if the outputs from the four lasers were combined into a single fiber.

There are a number of potential limitations to the study. First, the fitting approach for each technique was not the same at baseline and subsequent FiO$_2$ steps. That is, the H-NIRS fitting routine at baseline included five fitting parameters: HHb and HbO$_2$ concentrations, a water fraction, and two scattering parameters. In subsequent steps, the scattering variables and the water fraction were fixed to their baseline values. Similarly, the analysis of the baseline TR-NIRS data at each wavelength included μ_a, μ'_s and an amplitude factor, while in the following sets only μ_a was used as a fitting parameter. This approach was used to reduce the variability in the estimates of the parameters considering only blood oxygenation (i.e. absorption) should change during the hypoxic increments. The constancy of the water fraction in brain is well documented, and likewise the scattering property of tissue only changes under extreme conditions[51].

A second limitation is that this study did not include repeat measurements to assess reproducibility, as has been performed in clinical studies using commercial NIRS devices[26]. Typically, these studies involve repetitively placing the NIRS probes on the patient's head to acquire serial measurements. Practically, this would have been challenging to perform in these experiments given the small head size of the piglet head, which makes replicating probe placement challenging. However, given the encouraging results of this validation study, assessing precision in a clinical study using "place and replace" acquisitions is a logical next step.

Chapter 5

5 Summary
5.1 Future Work

As discussed in Chapter 4, a concern with the H-NIRS method was the underestimation of μ'_s relative to TR-NIRS. This requires further investigation to determine the cause of this error, such as potential cross-talk between the fitting parameters for the first derivative analysis. One approach would be to reanalyze the H-NIRS data with the added constraint of using a known μ'_s value measured by TR-NIRS. In addition, further experiments could be conducted using tissue mimicking phantoms consisting of a well characterized scattering medium (i.e. intralipid). While this set up would not replicate tissue oxygenation, it would provide a means of assessing the accuracy of the techniques for a simplified condition. An extension of this could combine intralipid with blood and altering the oxygen available to the hemoglobin to make measurements of oxygen saturation[55].

Despite the discrepancy in μ'_s values, this study demonstrated that H-NIRS could estimate StO_2 and therefore an immediate clinical aim will be to conduct a reproducibility study on a patient population in the neonatal intensive care unit. Similar to studies using commercial clinical NIRS systems, the precision of StO_2 measurements acquired by H-NIRS will be tested by performing place-and-replace acquisitions. As outlined in the Introduction, H-NIRS also provides the ability to monitor cytochrome oxidase and has been combined for DCS to monitor StO_2, CBF and CCO in an animal model of neonatal hypoxia ischemia. Another immediate clinical aim is, therefore, to monitor the interactions between these three parameters in preterm infants during the first few days of life, as this is the time window when the newborn is most vulnerable to IVH. A final clinical aim will be to measure StO_2 in preterm infants diagnosed with PHVD. Serial measurements leading up to, during and after treatment, such as by draining CSF through

ventricle tapping, could begin to assess the value of this technology in improving the management of this condition.

5.2 Conclusion

The work presented in this thesis demonstrated the accuracy of H-NIRS differential analysis to measure StO_2 over a range of oxygenation states in a piglet model of hypoxia. Validation was performed by comparisons to StO_2 measurements obtained with TR-NIRS, a technology that is considering the most accurate for measuring tissue optical properties. Good agreement between the two sets of measurements of μ_a and HHb concentration and StO_2 were found. However, the study also relieved a significant bias in μ'_s values from H-NIR, as well as higher variability in the measurements of HbO_2 concentration. Further investigation is required to determine the causes of these discrepancies. The precision of the H-NIRS StO_2 measurements were also examined and found to be comparable to those made using commercially available devices. The advantage of using H-NIRS is that the measurements are not limited to a few wavelengths, allowing for more information, primarily in terms of additional chromophores, to be extracted from a single acquisition. Derivative analysis removes DC components from the acquired signals that may arise from imperfect fiber coupling. Finally, one of the most attractive features of the H-NIRS system is the low cost and simplicity of the components. These results suggest that a H-NIRS system could be a valuable tool in the care of preterm infants suffering cerebral injuries like IVH and PHVD.

6   References

1. Malloy, M. H. Changes in infant mortality among extremely preterm infants: US vital statistics data 1990 vs 2000 vs 2010. *J. Perinatol. N. Y.* **35**, 885–890 (2015).

2. Johnston, K. M. *et al.* The economic burden of prematurity in Canada. *BMC Pediatr.* **14**, (2014).

3. Cherian, S., Whitelaw, A., Thoresen, M. & Love, S. The Pathogenesis of Neonatal Post-hemorrhagic Hydrocephalus. *Brain Pathol.* **14**, 305–311 (2006).

4. Vesoulis, Z. A. & Mathur, A. M. Cerebral Autoregulation, Brain Injury, and the Transitioning Premature Infant. *Front. Pediatr.* **5**, (2017).

5. Horbar, J. D. *et al.* Mortality and Neonatal Morbidity Among Infants 501 to 1500 Grams From 2000 to 2009. *PEDIATRICS* **129**, 1019–1026 (2012).

6. Synnes, A. R., Chien, L.-Y., Peliowski, A., Baboolal, R. & Lee, S. K. Variations in intraventricular hemorrhage incidence rates among Canadian neonatal intensive care units. *J. Pediatr.* **138**, 525–531 (2001).

7. Szpecht, D., Szymankiewicz, M., Nowak, I. & Gadzinowski, J. Intraventricular hemorrhage in neonates born before 32 weeks of gestation—retrospective analysis of risk factors. *Childs Nerv. Syst.* **32**, 1399–1404 (2016).

8. Holwerda, J. C. *et al.* Functional outcome at school age of neonatal post-hemorrhagic ventricular dilatation. *Early Hum. Dev.* **96**, 15–20 (2016).

9. Whitelaw, A., Thoresen, M. & Pople, I. Posthaemorrhagic ventricular dilatation. *Arch. Dis. Child. Fetal Neonatal Ed.* **86**, F72–F74 (2002).

10. Whitelaw, A. & Aquilina, K. Management of posthaemorrhagic ventricular dilatation. *Arch. Dis. Child. - Fetal Neonatal Ed.* **97**, F229–F233 (2012).

11. Whitelaw, A. & Lee-Kelland, R. Repeated lumbar or ventricular punctures in newborns with intraventricular haemorrhage. *Cochrane Database Syst. Rev.* (2017). doi:10.1002/14651858.CD000216.pub2

12. Kishimoto, J. *et al.* Preterm neonatal lateral ventricle volume from three-dimensional ultrasound is not strongly correlated to two-dimensional ultrasound measurements. *J. Med. Imaging* **3**, 046003 (2016).

13. Olischar, M. *et al.* Cerebrospinal fluid drainage in posthaemorrhagic ventricular dilatation leads to improvement in amplitude-integrated electroencephalographic activity. *Acta Paediatr.* **98**, 1002–1009 (2009).

14. Norooz, F. *et al.* Decompressing posthaemorrhagic ventricular dilatation significantly improves regional cerebral oxygen saturation in preterm infants. *Acta Paediatr.* **104**, 663–669 (2015).

15. Hielscher, A. H., Alcouffe, R. E. & Barbour, R. L. Comparison of finite-difference transport and diffusion calculations for photon migration in homogeneous and heterogeneous tissues. *Phys. Med. Biol.* **43**, 1285–1302 (1998).

16. Brazy, J. E., Lewis, D. V. & Mitnick, H. Oxygenation in Preterm Infants: 11

17. Wyatt, J. S., Delpy, D. T., Cope, M., Wray, S. & Reynolds, E. O. R. Quantification of cerebral oxygenation and hemodynamics in sick newborn infants by near infrared spectroscopy. *The Lancet* **328**, 1063–1066 (1986).

18. Kleiser, S. *et al.* Comparison of tissue oximeters on a liquid phantom with adjustable optical properties: an extension. *Biomed. Opt. Express* **9**, 86–101 (2017).

19. Dix, L. M. L., van Bel, F., Baerts, W. & Lemmers, P. M. A. Comparing near-infrared spectroscopy devices and their sensors for monitoring regional cerebral oxygen saturation in the neonate. *Pediatr. Res.* **74**, 557–563 (2013).

20. Alderliesten, T. *et al.* Reference values of regional cerebral oxygen saturation during the first 3 days of life in preterm neonates. *Pediatr. Res.* **79**, 55 (2015).

21. Kurth, C. D., McCann, J. C., Wu, J., Miles, L. & Loepke, A. W. Cerebral Oxygen Saturation-Time Threshold for Hypoxic-Ischemic Injury in Piglets: *Anesth. Analg.* **108**, 1268–1277 (2009).

22. Kurth, C. D., Levy, W. J. & McCann, J. Near-Infrared Spectroscopy Cerebral Oxygen Saturation Thresholds for Hypoxia–Ischemia in Piglets. *J. Cereb. Blood Flow Metab.* **22**, 335–341 (2002).

23. Hou, X. *et al.* Research on the relationship between brain anoxia at different regional oxygen saturations and brain damage using near-infrared spectroscopy. *Physiol. Meas.* **28**, 1251 (2007).

24. Sorensen, L. C. & Greisen, G. Precision of measurement of cerebral tissue oxygenation index using near-infrared spectroscopy in preterm neonates. *J. Biomed. Opt.* **11**, 054005 (2006).

25. Plomgaard, A. M. *et al.* The SafeBoosC II randomized trial: treatment guided by near-infrared spectroscopy reduces cerebral hypoxia without changing early biomarkers of brain injury. *Pediatr. Res.* **79**, 528–535 (2016).

26. Jenny, C. *et al.* Reproducibility of cerebral tissue oxygen saturation measurements by near-infrared spectroscopy in newborn infants. *J. Biomed. Opt.* **16**, 097004 (2011).

27. Hyttel-Sorensen, S. *et al.* Cerebral near infrared spectroscopy oximetry in extremely preterm infants: phase II randomised clinical trial. *The BMJ* **350**, g7635 (2015).

28. David A. Boas, Constantinos Pitris, Nimmi Ramanujam. *Handbook of Biomedical Optics*. (Taylor & Francis Group, 2011).

29. Matcher, S. J., Cope, M. & Delpy, D. T. Use of the water absorption spectrum to quantify tissue chromophore concentration changes in near-infrared spectroscopy. *Phys. Med. Biol.* **39**, 177–196 (1994).

30. Wang, L. V. & Wu, H. *Biomedical Optics*. (John Wiley & Sons, Inc, 2012).

31. Jones, B., Hesford, C. M. & Cooper, C. E. The Use of Portable NIRS to Measure Muscle Oxygenation and Haemodynamics During a Repeated Sprint Running Test. in *Oxygen Transport to Tissue XXXV* (eds. Van Huffel, S., Naulaers, G., Caicedo, A., Bruley, D. F. & Harrison, D. K.) 185–191 (Springer New York, 2013).

32. Li, T., Duan, M., Li, K., Yu, G. & Ruan, Z. Bedside monitoring of patients with shock using a portable spatially-resolved near-infrared spectroscopy. *Biomed. Opt. Express* **6**, 3431–3436 (2015).

33. Greisen, G., Andresen, B., Plomgaard, A. M. & Hyttel-Sørensen, S. Cerebral oximetry in preterm infants: an agenda for research with a clear clinical goal. *Neurophotonics* **3**, 031407 (2016).

34. Matcher SJ, Kirspatrick PJ, Nahid K, et al. Absolute quantification methods in tissue near-infrared spectroscopy. (1995).

35. Jacques, S. L. Optical properties of biological tissues: a review. *Phys. Med. Biol.* **58**, R37 (2013).

36. Hessel, T. W., Hyttel-Sorensen, S. & Greisen, G. Cerebral oxygenation after birth - a comparison of INVOS ® and FORE-SIGHT™ near-infrared spectroscopy oximeters. *Acta Paediatr.* **103**, 488–493 (2014).

37. Chance, B. *et al.* Comparison of time-resolved and -unresolved measurements of deoxyhemoglobin in brain. *Proc. Natl. Acad. Sci.* **85**, 4971–4975 (1988).

38. Delpy, D. T. *et al.* Estimation of optical pathlength through tissue from direct time of flight measurement. *Phys. Med. Biol.* **33**, 1433–1442 (1988).

39. Kienle, A. & Patterson, M. S. Improved solutions of the steady-state and the time-resolved diffusion equations for reflectance from a semi-infinite turbid medium. *J. Opt. Soc. Am. A* **14**, 246–254 (1997).

40. Diop, M., Kishimoto, J., Toronov, V., Lee, D. S. C. & St. Lawrence, K. Development of a combined broadband near-infrared and diffusion correlation system for monitoring cerebral blood flow and oxidative metabolism in preterm infants. *Biomed. Opt. Express* **6**, 3907 (2015).

41. Diop, M., Wright, E., Toronov, V., Lee, T.-Y. & Lawrence, K. S. Improved light collection and wavelet de-noising enable quantification of cerebral blood flow and oxygen metabolism by a low-cost, off-the-shelf spectrometer. *J. Biomed. Opt.* **19**, 057007–057007 (2014).

42. Yeganeh, H. Z. *et al.* Broadband continuous-wave technique to measure baseline values and changes in the tissue chromophore concentrations. *Biomed. Opt. Express* **3**, 2761 (2012).

43. McLachlan, P. J. *et al.* Investigating the effects of cerebrospinal fluid removal on cerebral blood flow and oxidative metabolism in infants with post-hemorrhagic ventricular dilatation. *Pediatr. Res.* **82**, 634–641 (2017).

44. Pucci, O., Toronov, V. & Lawrence, K. S. Measurement of the optical properties of a two-layer model of the human head using broadband near-infrared spectroscopy. *Appl. Opt.* **49**, 6324–6332 (2010).

45. Rajaram, A. *et al.* Simultaneous monitoring of cerebral perfusion and cytochrome c oxidase by combining broadband near-infrared spectroscopy and diffuse correlation spectroscopy. *Biomed. Opt. Express* **9**, 2588 (2018).

46. Bale, G., Elwell, C. E. & Tachtsidis, I. From Jöbsis to the present day: a review of clinical near-infrared spectroscopy measurements of cerebral cytochrome-c-oxidase. *J. Biomed. Opt.* **21**, 091307 (2016).

47. Mamadou Diop *et al.* Time-resolved near-infrared technique for bedside monitoring of absolute cerebral blood flow. in **7555**, 75550Z-7555–9 (2010).

48. Diop, M., Elliott, J. T., Tichauer, K. M., Lee, T.-Y. & St. Lawrence, K. A broadband continuous-wave multichannel near-infrared system for measuring regional cerebral

blood flow and oxygen consumption in newborn piglets. *Rev. Sci. Instrum.* **80**, 054302 (2009).

49. Diop, M. & Lawrence, K. S. Deconvolution method for recovering the photon time-of-flight distribution from time-resolved measurements. *Opt. Lett.* **37**, 2358 (2012).

50. Vasilis Ntziachristos, Arjun G. Yodh & Britton Chance. Accuracy limits in the determination of absolute optical properties using time-resolved NIR spectroscopy. in **3597**, 3597–10 (1999).

51. G Zhang and A Katz and R R Alfano and A D Kofinas and D A Kofinas and P G Stubblefield and W Rosenfeld and D Beyer and D Maulik and M R Stankovic. Brain perfusion monitoring with frequency-domain and continuous-wave near-infrared spectroscopy: a cross-correlation study in newborn piglets. *Phys. Med. Biol.* **45**, 3143 (2000).

52. Ijichi, S. *et al.* Quantification of cerebral hemoglobin as a function of oxygenation using near-infrared time-resolved spectroscopy in a piglet model of hypoxia. *J. Biomed. Opt.* **10**, 024026–0240269 (2005).

53. SafeBoosC-III. Available at: https://www.rigshospitalet.dk/english/departments/juliane-marie-centre/department-of-neonatology/research/SafeboosC-III/Sider/default.aspx. (Accessed: 28th August 2018)

54. Dullenkopf, A., Frey, B., Baenziger, O., Gerber, A. & Weiss, M. Measurement of cerebral oxygenation state in anaesthetized children using the INVOS 5100 cerebral oximeter. *Pediatr. Anesth.* **13**, 384–391 (2003).

55. Kleiser, S., Nasseri, N., Andresen, B., Greisen, G. & Wolf, M. Comparison of tissue oximeters on a liquid phantom with adjustable optical properties. *Biomed. Opt. Express* **7**, 2973 (2016).

56. Demel, A., Wolf, M., Poets, C. F. & Franz, A. R. Effect of different assumptions for brain water content on absolute measures of cerebral oxygenation determined by frequency-domain near-infrared spectroscopy in preterm infants: an observational study. *BMC Pediatr.* **14**, (2014).

Curriculum Vitae

Name: Matthew Kewin

Post-secondary   Western University
Education and   London, Ontario, Canada
Degrees: 2012-2016 BM.Sc.

                      The University of Western Ontario
                      London, Ontario, Canada
                      2016-2018 M.Sc.

Honours and   Western Graduate Research Scholarship
Awards: 2016-2018

                      Dean's Honour roll – Western University
                      2014,2015

Related Work   Teaching Assistant
Experience   The University of Western Ontario
                      1993-1995

Publications:

A. Rajaram, G. Bale, **M. Kewin**, L. Morrison, I. Tachtsidis, K. St Lawrence, M. Diop. Simultaneous monitoring of cerebral perfusion and cytochrome c oxidase by combining broadband near-infrared spectroscopy and diffuse correlation spectroscopy. Biomedical Optics Express. 2018

Oral Presentations:

M. Kewin, D. Milej, A. Abdalmalak, A. Rajaram, M. Diop, S. de Reibaupierre, K. St Lawrence. Validation of a hyperspectral NIRS method for measuring oxygen saturation by comparison to Time-Resolved NIRS. Biophotonics Congress: Biomedical Optics 2018

Poster Presentaions:

M.Kewin, D. Milej, A. Abdalmalak, A. Rajaram, M.Diop, S. de Ribaupierre, K. St Lawrence. Comfirmation of Derivative Hyperspectral NIRS Method for Measuring Oxygen Saturation by Comparison to Time-Resolved NIRS. London Health Research Day. 2018

M.Kewin, D. Milej, A. Abdalmalak, A. Rajaram, M.Diop, S. de Ribaupierre, K. St Lawrence. Comfirmation of Derivative Hyperspectral NIRS Methods to Measure Oxygen Saturation by Comparison to established Time-Resolved NIRS. 16th Annual Meeting of Imaging Network Ontario. 2018

M. Kewin, U. Anazodo, J. Thiessen, J. Butler, J. Hadaway, L.Morrison, F.Prato, R.T. Thompson, K. St Lawrence. Evaluation of Recovery Coefficients Applied to Image Derived Input Functions for Patlak Analysis of FDG-PET MRI.TBD. 15th Annual Meeting of Imaging Network Ontario. 2017

M. Kewin, U Anazodo, J Thiessen, J Butler, J Hadaway, L Morrison, FS Prato, RT Thompson, K St. Lawrence. (2016). Evaluation of MR image-derived input function methods for quantification of glucose metabolism by integrated PET-MRI. PSMR- 5th International Conference on PET/MR and SPECT/ MR, Cologne, Germany 2016

U. Anazodo, **M. Kewin**, E Finger, J. Thiessen, J. Hadway, J. Butler,W. Pavlosky, F. Prato, R.T. Thompson, K.St Lawrence. Preliminary evaluation of MRI-derived input function for quantitative measurement of glucose metabolism in an integrated PETMRI. PSMR 2015: 4th International Conference on PET/MR and SPECT/MR, Elba Island, Italy. 2015